Applied Thermal Engineering 259 (2025) 124861

Contents lists available at ScienceDirect

Applied Thermal Engineering

journal homepage: www.elsevier.com/locate/apthermeng

Research Paper

Geothermal system lifetime with fracture heterogeneity and thermal nonequilibrium impact

Zijun Wei [a,b], Ke Gao [b,*], Sanbai Li [c,*]

[a] School of Environment, Harbin Institute of Technology, Harbin, China
[b] Department of Earth and Space Science, Southern University of Science and Technology, Shenzhen, China
[c] School of Resources and Safety Engineering, Central South University, Changsha, China

ARTICLE INFO

Keywords:
Enhanced geothermal systems
Thermo-hydro-mechanical model
Fractures' heterogeneity
Local thermal equilibrium
Local thermal non-equilibrium

ABSTRACT

Geothermal energy is a clean and sustainable alternative energy, and enhanced geothermal systems are an essential technology offering an industrial-scale method to tap geothermal energy. This technology stimulates numerous reservoir fractures, creating primary flow channels for fluids to extract heat. The important question of how the permeability of fracture swarm evolves during fluid circulation and how this evolution potentially affects the geothermal system life remains to be further answered. To address this, we develop and validate a fully coupled thermo-hydro-mechanical model based on the discrete fracture network. Results show a positive feedback mechanism between pore pressure/temperature changes and fracture permeability evolution, leading to monotone permeability-increasing in a limited number of specific fractures, indicating uneven permeability evolution of fracture swarm is crucial in shortening reservoir lifetime. Furthermore, we conduct a comparative analysis of multiple factors to determine what most significantly affects reservoir lifetime, including fracture heterogeneity, the local thermal non-equilibrium effect, and layout strategies. Results indicate the strong heterogeneity of the fracture network is dominant, and the inherent heterogeneity of hydraulic fractures is further exacerbated during geothermal production. Neglecting fractures' mechanical response leads to an overestimated outcome. A simplified thermal-hydraulic analysis indicates a 34 % higher temperature and a 6 % higher heat extraction rate than the coupled thermo-hydro-mechanical modeling. In contrast, the impact of the local thermal non-equilibrium effect is negligible, with comparable results between equilibrium and non-equilibrium models. We further find the multi-well layout can effectively suppress the heterogeneity impact and prevent preferential flow paths. Compared to dual-well systems, the multi-well scheme has a 24 % higher temperature and a 6 % higher heat extraction rate.

1. Introduction

Pursuing clean and sustainable energy becomes an effective means for humanity to combat climate warming. Geothermal energy emerges as a promising alternative due to its worldwide availability and vast exploitation potential. Researchers estimated the geothermal energy potential in the United States is approximately 1.4×10^{25} J, assuming a 2 % conservative recovery rate, and could provide energy nearly 3000 times the annual energy consumption [1]. Similarly, the Chinese Academy of Sciences estimates China's geothermal resource base at 2.1×10^{25} J, capable of meeting energy demands 4400 times its annual consumption [2]. Deep geothermal exploitation focuses on hot dry rock (HDR) resources, which refer to the rock strata located 3–10 km beneath the Earth's surface, characterized by high temperatures yet low porosity and permeability [3]. The target reservoir temperature for HDR exploitation is about 150–250 °C [4,5].

The geothermal exploitation engineering discussed here specifically refers to enhanced geothermal systems (EGS), a large-scale method for converting geothermal resources into electricity. EGS employs artificial fracturing to create fractures in low-permeability formations, and fluids extract heat through a closed-loop system composed of injection/production wells and fractures [6].

Existing EGS numerical models can be roughly categorized into three types: the Equivalent Continuum Model (ECM), the Discrete Fracture Model (DFM), and the Hybrid Discrete-Continuum Model [7]. The

Abbreviations: EGS, enhanced geothermal systems; HDR, hot dry rock; THM, thermo-hydro-mechanical; TH, thermal-hydraulic; LTE, local thermal equilibrium; LTNE, local thermal non-equilibrium.

* Corresponding authors.
E-mail addresses: gaok@sustech.edu.cn (K. Gao), lisb6@csu.edu.cn (S. Li).

https://doi.org/10.1016/j.applthermaleng.2024.124861
Received 24 July 2024; Received in revised form 25 October 2024; Accepted 7 November 2024
Available online 13 November 2024

Nomenclature

ρ_m	density of rock mass, kg/m^3
ρ_s	density of solid matrix, kg/m^3
ρ_f	density of fluid, kg/m^3
p	pore pressure, Pa
b	Biot coefficient
S	water storage coefficient of porous matrix, Pa^{-1}
S_f	water storage coefficient of fracture, Pa^{-1}
c_s	compressibility of solid matrix, Pa^{-1}
c_f	compressibility of fluid, Pa^{-1}
ε_{vol}	volumetric strain
ϕ	porosity of porous matrix
ϕ_f	porosity of fracture
d_f	fracture width, m
α_m	thermal expansion coefficient of rock mass, K^{-1}
α_s	thermal expansion coefficient of solid matrix, K^{-1}
α_f	thermal expansion coefficient of fluid, K^{-1}
k	permeability of porous matrix, m^2
k_f	permeability of fracture, m^2
μ	dynamic viscosity of fluid, Pa·s
$C_{p,s}$	isobaric heat capacity of solid matrix, J/kg/K
$C_{p,f}$	isobaric heat capacity of fluid, J/kg/K
k_{eff}	thermal conductivity of mass rock, W/m/K
q_{sf}	interphase convective heat transfer coefficient, W/m^3/K
m	constitutive constant of fracture's permeability, Pa^{-1}
T	current temperature of reservoir, K
T_0	initial temperature of reservoir, K
T_{in}	temperature of the injected fluid, K
Q	mass source or sink, kg/m^3/s
Q_T	heat source or sink, W/m^3

Tensor/Vector Signs

$\boldsymbol{\sigma}$	total stress tensor, Pa
$\mathbf{C}$	stiffness matrix, Pa
$\boldsymbol{\varepsilon}$	total strain tensor
$\boldsymbol{\varepsilon}_{th}$	thermal strain tensor
$\mathbf{s}$	displacement vector, m
$\mathbf{g}$	gravity acceleration vector, m/s^2
$\mathbf{u}$	seepage velocity within porous matrix, m/s
$\mathbf{u}_f$	seepage velocity within fracture, m/s

fundamental difference lies in whether reservoir fractures are characterized explicitly, making these different models suitable for varying engineering needs. The ECM method is suitable for simulating large-scale fluid flow and heat transfer processes, where characterizing all reservoir fractures is impractical. The DFM method focuses on rock engineering design for near-field problems [8]. The hybrid model finds itself in the middle ground by employing DFM to simulate hydraulic fractures in the area of interest while utilizing ECM to model continuously distributed microfractures in the far field [9,10]. However, it is complicated by the need to communicate flow and transport properties between the model's subdomains [11].

The ECM method homogenizes the entire fracture-distributed domain into an equivalent porous medium. It can be further categorized into single-porosity models [12,13], dual-porosity models [14,15], and multi-porosity models [16]. Jiang et al. [12] used the single-porosity method to develop a coupled thermal-hydraulic (TH) model and evaluated heat extraction performance for various well configurations. However, they overlooked the mechanical behavior of the rock matrix and fractures. Cao et al. [13] improved by incorporating the relationship between effective stress and permeability, establishing a coupled thermo-hydro-mechanical (THM) model that reflects the rock's mechanical behavior. Gelet et al. [14] extended the dual-porosity approach in EGS by introducing a generalized framework. Taron et al. [15] utilized the dual-porosity model to investigate the variations in permeability within a typical geothermal reservoir, considering the intricate coupled effects of thermo-hydro-mechanical-chemical (THMC) fields. Furthermore, Wu et al. [16] introduced a multi-porosity model dividing rock mass into matrix blocks, large fractures, and micro-fractures. These systems work independently and interactively, allowing the multi-continuum approach to capture rock heterogeneity to some extent.

While the above ECM methods simplify calculations by avoiding fractures' explicit representation, they overlook the significant impact of complex fracture configurations and connectivity. Therefore, they may fail to address the multi-scale seepage process in fractured reservoirs [17]. Moreover, continuum methods are typically suited for reservoirs of uniformly distributed fractures, which may contradict the real-world highly uneven fracture distributions. For example, a granite uranium mine in Fanay-Augères exhibited a four-order-of-magnitude difference between the largest and smallest injection flow rates [18]. Casas et al. [19] found that the strong heterogeneity and channeling govern fluid flow and transport behavior overwhelmingly. Some studies [20–22] further demonstrated even a geometrically well-connected fracture network could exhibit sparse flow paths if fracture conductivity varies widely. Consequently, when simulating fractures as the primary flow channels, the ECM methods are prone to significant errors. Finally, continuum models can't reflect permeability changes due to fracture deformation. Given these reasons, DFM methods garner increasing attention due to their ability to represent fractures explicitly.

The DFM methods contain the Discrete Fracture Network (DFN) and the Embedded Discrete Fracture Model (EDFM). Both approaches explicitly define fractures and establish mass transport equations for the matrix and fractures separately. EDFM's difficulty lies in the characterization methodology for the interaction between discrete fracture grids and spatially intersecting matrix grids [23]. Instead, in the finite element-based DFN approach, fractures are conceptualized as natural boundary conditions imposed on matrix blocks. This approach represents the fluid interaction in a more general mathematical form [24], serving as a reference for adopting the DFN method in our subsequent modeling. Based on the DFN model, Sun et al. [25] conduct a coupled THM simulation for highly fractured two-dimensional (2D) reservoirs. Later, they extended this approach to a three-dimensional (3D) version [26]. However, this 3D version only accounted for a single fracture's impact. Yao et al. [27] further developed a 3D complex fracture network to assess the thermal production performance of the Desert Peak project. Similarly, Lei et al. [28] developed a DFN model to evaluate the heat extraction performance in the geothermal project located in the Gonghe Basin, Northwest China.

An enormous research focuses on investigating the impact of various parametric conditions on exploitation performance. For example, the number of fractures and fracture spacing [29], different working fluids (such as CO_2 and water) [30], or various injection flow rates [31]. However, we believe beyond these externally regulated factors, the reservoir's internal characteristics may be the decisive factor influencing production performances. Unfortunately, researchers [28,32,33] often assume a uniform width for fracture swarm, and the intrinsic heterogeneity of fractures is obscured. Cacas et al. [19] and Hyman [34] emphasized the importance of heterogeneity, yet they overlooked fractures' further deformation during the production phase. In other words, they did not address how the heterogeneity would further evolve caused by mining. Given this knowledge gap, we aim to investigate how fractures' inherent heterogeneity will further develop during fluid

circulation and how it potentially affects the EGS lifetime.

Additionally, we note that there are two widely used heat transfer frameworks: local thermal equilibrium (LTE) and local thermal non-equilibrium (LTE). Groundwater flow is considered a slow flow phenomenon typically, allowing sufficient heat exchange time between water and rock. This rationale provides the basis for employing the LTE hypothesis [35,36]. However, the EGS scenario is somewhat unique. The porous structure often contains numerous fractures, and the flow within these fractures may be rapid rather than slow seepage. Consequently, some studies argue that the LTNE theory offers a more realistic representation of the heat exchange dynamics [25–27].

Wang et al. [32] and Jiang et al. [35] applied and recommended the LTNE hypothesis to address EGS problems, unfortunately, these recommendations [25–27,32,35] were not based on a thorough LTE-LTNE comparison. In fact, some analyses suggested the LTE assumption is reasonable because the observed temperature difference between rock and fluid in LTNE is small enough [37,38]. The critical view is that there is a difference in the thermal breakthrough time between the two theories, and the LTNE impact becomes significant as the interphase heat transfer coefficient q_{sf} decreases [39]; however, it should be noted that extremely small transfer coefficients were adopted in this study. Hamidi et al. [40] pointed the LTNE influence is dependent on the reservoir's porosity and permeability properties, with an approximately 2 % average temperature difference in the simulated domain.

What draws our attention is these models [37–41] lack realism to some degree, as they deal not with typical fractured reservoirs but with conclusions derived from continuum models. Specifically, the HDR fractured reservoir is idealized as a single-porosity saturated medium [41]. As previously elaborated, the continuum method has limitations in characterizing fractured reservoirs' speeage behavior. We believe that an LTNE analysis based on directly and explicitly representing fractures, rather than substituting them with an equivalent continuum, is more appropriate for EGS scenarios. Knowledge in this area urgently needs further supplementation and refinement. Consequently, our work incorporates fractures explicitly and considers differential seepage between fractures and matrix, to explore whether the LTNE effect will have a more significant impact in combination with the rapid fracture seepage process. Another regrettable aspect is studies employing the LTNE framework frequently disregard the specific values of the water-rock heat transfer coefficient. Some studies [32,35,39] artificially select a smaller coefficient (e.g., ranging from 0.001 to 1.0 W/m^3/K) to enhance the LTNE phenomenon. Consequently, we believe a specific evaluation of this coefficient is needed. Finally, to investigate whether the LTNE effect is a key factor affecting the EGS lifetime, we conduct a multi-factor comparative analysis and explore what priority should be given to LTNE. The scope of discussion is limited to fracture heterogeneity, the local thermal non-equilibrium effect, and various layout strategies, as shown in Fig. 1.

This paper is structured as follows. In Section 2, we introduce the governing systems and the implementation methods of the coupled THM model. In Section 3, we validate the model against two benchmark models. In Section 4, we perform numerical investigations based on the 3D geothermal extraction model. In Section 5, we compare and discuss different factors that affect geothermal extraction. Finally, in Section 6, we provide a summary of the main findings of this work.

2. Methods

The fully coupled THM mathematical model includes the governing equations and the corresponding initial conditions and boundary conditions. Before introducing the specific set of control equations required, it is necessary to explain some of the prerequisite assumptions adopted in the mathematical model. (1) The rock mass exhibits isotropic behavior, adhering to the thermo-poroelastic law and the principle of effective stress. (2) The geothermal system is assumed to be a single-phase fluid system, employing water as the working fluid, and the rock mass is a saturated porous medium during fluid circulation. (3) The water is assumed to be nearly incompressible, thus its thermo-physical properties are hypothesized to depend solely on temperature. (4) The potential phase change of water is ignored.

2.1. Momentum balance equations

For deformable porous media, the displacement field can be calculated based on Newton's second law. Under quasi-static assumptions (ignoring the acceleration term), the momentum balance equations of the system can be expressed as

$$\nabla\cdot\boldsymbol{\sigma}+\rho_m\mathbf{g}=\mathbf{0} \tag{1}$$

where $\boldsymbol{\sigma}$ represents the total stress tensor; $\rho_m=\phi\rho_f+(1-\phi)\rho_s$ represents the density of rock mass; ϕ is the porosity; ρ_f and ρ_s denote the density of fluid phase and solid phase, respectively; $\mathbf{g}$ is the gravity acceleration vector. The principle of effective stress indicates that the rock skeleton and pore fluid bear the total stress together. Hooke's law relates the relationship between a rock skeleton's mechanical stress and displacement, and the Biot coefficient gives the weight of the fluid sharing the total stress, i.e.,

$$\boldsymbol{\sigma}=\boldsymbol{C}:(\boldsymbol{\varepsilon}-\boldsymbol{\varepsilon}_{th})-bp\boldsymbol{I} \tag{2}$$

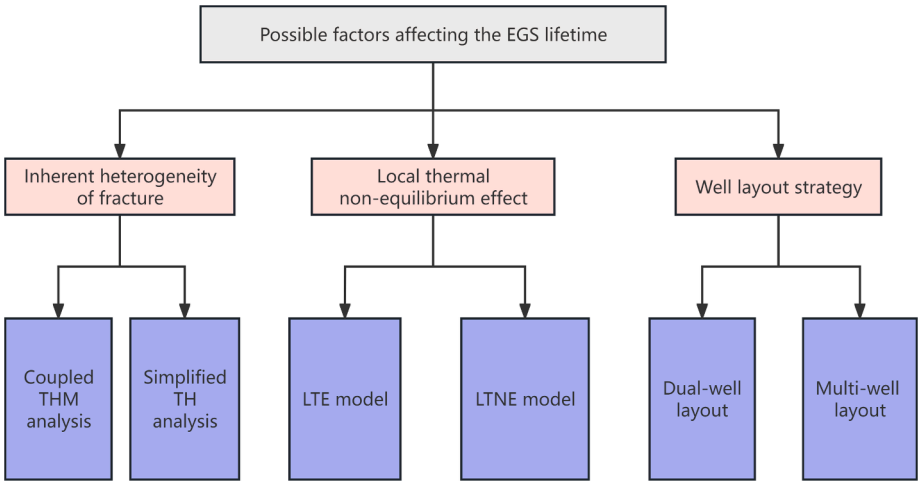

Fig. 1. Flow diagram for the case study.

where $\mathbf{C}$ is the material stiffness matrix; $\boldsymbol{\varepsilon}$ is the total strain tensor following the form $\boldsymbol{\varepsilon} = \frac{1}{2}(\nabla \boldsymbol{s} + (\nabla \boldsymbol{s})^{\mathrm{T}})$ under the infinitesimal deformation assumption; $\mathbf{s}$ is the displacement vector; $\boldsymbol{\varepsilon}_{th} = \alpha_m(T - T_0)\boldsymbol{I}$ is the thermal strain tensor; T and T_0 represents the current temperature and initial temperature, respectively; $\mathbf{I}$ is the identity matrix; b is the Biot coefficient; p is the pore pressure.

2.2. Mass balance equations

For fractured porous media, due to the significant differences in porosity and permeability properties between the matrix and fractures, it is necessary to define seepage equations for the matrix and fractures separately. The influence of structural deformation and temperature changes on the pore pressure is taken into account based on the thermo-poroelastic law [42], correspondingly, the governing equation to the matrix nodes has the following form [36,43],

$$\rho_f S\frac{\partial p}{\partial t} + \nabla\cdot(\rho_f \mathbf{u}) = -b\rho_f\frac{\partial \varepsilon_{vol}}{\partial t} + 3\rho_f\alpha_m\frac{\partial T}{\partial t} + Q \tag{3}$$

where S is the water storage coefficient of the matrix, i.e., $S = \phi c_f + (1-\phi)c_s$, reflecting the compressibility of the saturated rock mass; c_f and c_s represent the compressibility of fluid and solid phases, respectively; ε_{vol} is the volumetric strain; $\alpha_m = \phi\alpha_f + (1-\phi)\alpha_s$ is the linear thermal expansion coefficient of rock mass; α_f and α_s represent the thermal expansion coefficient of fluid and solid phases, respectively; Q refers to external mass sources or sinks. The seepage velocity $\mathbf{u}$ is determined by the Darcy's law, i.e.,

$$\boldsymbol{u} = -\frac{k}{\mu}(\nabla p - \rho \boldsymbol{g}) \tag{4}$$

where k is the permeability of the porous matrix, and μ is the dynamic viscosity of the fluid.

Compared to fractures whose dimensions, specifically height and length, are measured in meters, hydraulic fractures exhibit a significantly narrower width, typically measured in millimeters [28]. Therefore, fluid flow along the width within the internal fracture can be overlooked. As a result, the seepage behavior within the fracture can be simplified as a 2D flow along its tangential direction. Consequently, the governing equation to the fracture nodes has the following form [36],

$$d_f\rho_f S_f\frac{\partial p}{\partial t} + \nabla_t\cdot(d_f\rho_f \mathbf{u}_f) = -d_f\rho_f b\frac{\partial \varepsilon_{vol}}{\partial t} + 3d_f\rho_f\alpha_m\frac{\partial T}{\partial t} + \rho_f \boldsymbol{u}\cdot\boldsymbol{n} \tag{5}$$

$$\boldsymbol{u}_f = -\frac{k_f}{\mu}(\nabla_t p - \rho_f \boldsymbol{g}) \tag{6}$$

where d_f represents the fracture width; S_f is the water storage coefficient of fracture (contrary to the properties of porous matrix, fractures are generally considered as high permeability and low water storage capacity, meaning $S_f << S$); ∇_t represents the tangential derivative; $\mathbf{u}_f$ represents the flow velocity inside the fracture determined by the tangential version of Darcy's law, e.g., Eq. (6); k_f represents the permeability of fractures. In COMSOL Multiphysics®, the discrete fractures are described using interior boundaries, which means that the outgoing mass flux $\rho_f \boldsymbol{u}\cdot\boldsymbol{n} = -\rho_f\frac{k}{\mu}\frac{\partial p}{\partial n}$ leaves the porous matrix domain and is captured by the adjacent fracture thin layer modeled as a boundary. This process is reflected in Eq. (5) in a source term form.

2.3. Energy balance equations

There are two predominant assumptions in the treatment of energy conservation equations in geothermal simulations, namely the LTE and LTNE assumptions. The LTE hypothesis assumes that when fluid flows through pores or fractures, the heat exchange between the fluid and the rock is so good that the temperatures of the fluid and the solid phase can be considered equal at any given location and time point. This assumption makes the mathematical model more concise. However, it may fail to accurately capture temperature differences in cases of high flow velocity or poor rock thermal conductivity. In contrast, the LTNE hypothesis recognizes there could be temperature differences between fluid and rock. Although this hypothesis increases complexity, proponents of this theory argue that it offers a precise depiction of heat exchange dynamics between fluid and rock.

2.3.1. Local thermal equilibrium assumption

Under the LTE framework, we only need one equation to describe the temperature of the entire porous structure. Based on mixing law, the heat transfer equations' forms are very similar to the seepage field equations, i.e., Eqs. (3) and (5). Specifically, for the porous matrix nodes, the heat transfer equation can be described using the following formula [44,45],

$$(\rho C_p)_{eff}\frac{\partial T}{\partial t} + \rho_f C_{p,f}\boldsymbol{u}\cdot\nabla T + \nabla\cdot(-k_{eff}\nabla T) = Q_T \tag{7}$$

where $(\rho C_p)_{eff} = \phi\rho_f C_{p,f} + (1-\phi)\rho_s C_{p,s}$ represents the effective volumetric heat capacity of the porous structure; $C_{p,f}$ and $C_{p,s}$ denote the isobaric heat capacity of the fluid and solid phases, respectively; $\mathbf{u}$ is the Darcy seepage velocity within the matrix; $k_{eff} = \phi k_f + (1-\phi)k_s$ represents effective thermal conductivity of the porous structure; k_f and k_s denote the thermal conductivity of the fluid and solid phases, respectively; Q_T is the volume heat source strength.

Analogously, for the fracture nodes, the heat transfer equation has the following form [45],

$$d_f(\rho C_p)_{eff}\frac{\partial T}{\partial t} + d_f\rho_f C_{p,f}\boldsymbol{u}_f\cdot\nabla_t T + \nabla_t\cdot(-d_f k_{eff}\nabla_t T) = d_f Q_T + \boldsymbol{q}\cdot\boldsymbol{n} \tag{8}$$

where $\boldsymbol{q}\cdot\boldsymbol{n}$ is the heat exchange flux between fracture and matrix determined by Fourier's law, i.e., $\boldsymbol{q} = -k_{eff}\nabla T$. In the coupling relation between fracture and matrix, the outgoing heat flux $\boldsymbol{q}\cdot\boldsymbol{n}$ leaves the porous matrix domain and is received in the source term by the adjacent fracture thin layer modeled as a boundary.

2.3.2. Local thermal non-equilibrium assumption

The LTNE approach requires the energy balance of the liquid and solid phases must be considered separately, and the corresponding heat exchange must be explicitly defined. This approach uses two energy equations for each phase of the porous medium that solves for two temperature fields. It numerically doubles the number of freedoms to solve but provides a general frame for heat transfer in porous media. The energy balance equations for solid and fluid phases are as follows [44],

$$(1-\phi)\rho_s C_{p,s}\frac{\partial T_s}{\partial t} + (1-\phi)\nabla\cdot(-k_s\nabla T_s) = q_{sf}(T_f - T_s) + (1-\phi)Q_s \tag{9}$$

$$\phi\rho_f C_{p,f}\frac{\partial T_f}{\partial t} + \rho_f C_{p,f}\boldsymbol{u}\cdot\nabla T_f + \nabla\cdot(-\phi k_f\nabla T_f) = q_{sf}(T_s - T_f) + \phi Q_f \tag{10}$$

where T_s and T_f denote solid phase temperature and fluid phase temperature, respectively; Q_s and Q_f are the solid and fluid volume heat sources, respectively; q_{sf} is the interphase convective heat transfer coefficient. It should be noted that Eqs. (9) and (10) are achieved by adding two porous medium heat transfer modules in COMSOL Multiphysics®, i.e., the exchanged opposite heat sources $q_{sf}(T_f - T_s)$ and $q_{sf}(T_s - T_f)$ that one phase receives from or releases to the other when respective temperatures differ, are assigned separately. At the same time, porosity attributes need to be assigned to both matrix grid nodes and fracture grid nodes separately, and the seepage velocity on matrix nodes and fracture nodes comes from the coupling relationship with the seepage field, i.e., Eqs. (3) and (5). Further, the average temperature of the porous structure can be estimated as [46]

$$T = \frac{\phi\rho_f C_{p,f} T_f + (1-\phi)\rho_s C_{p,s} T_s}{\phi\rho_f C_{p,f} + (1-\phi)\rho_s C_{p,s}} \tag{11}$$

2.4. Coupling relationship and implementation

EGS is a comprehensive multiphysics coupling system. Besides the direct coupling relationships, which refer to the mutual contributions among multiple field equations, such as thermal convection or thermal expansion effects, there are also indirect coupling relationships. For instance, fluid injection may alter pore structure, thereby affecting structural permeability. In addition, the thermal properties of the fluid may be influenced by other field variables during the flow process.

As the calculation of the stress field is based on the assumption of infinitesimal deformation, changes in the porosity and permeability of the porous matrix are ignored here. Instead, we focus on the changes in fracture permeability caused by variations in its stress conditions [47], e.g.,

$$k_f = k_0 \exp(m\sigma_n) \tag{12}$$

where m is a normalizing constant. In this paper, the value of the constitutive constant is set as 1.0×10^{-7} Pa^{-1}, which is referenced from the calibration in relevant literature [26,48]. σ_n represents the effective normal stress acting on the fracture; k_0 is the initial permeability before the fracture is disturbed, which can be estimated by the cubic law,

$$k_0 = \frac{d_f^2}{12} \tag{13}$$

In this work, water is used as a working fluid due to its easy accessibility and favorable heat recovery performance. In a typical EGS, the temperature of the injected fluid can deviate from the reservoir temperature by several hundred degrees Celsius. Consequently, the thermophysical properties of the working fluid could undergo significant variations throughout the flow process. Therefore, a comprehensive mathematical model is necessary for describing the fluid's state equation. Specifically, the state equation for water can be expressed as a function of temperature [49],

$$\rho_w = 838.466 + 1.401T - 0.003T^2 + 3.718 \times 10^{-7}T^3, T \in [293K, 550K] \tag{14}$$

$$C_{pw} = 12010.2 - 80.4T + 0.3T^2 - 5.4 \times 10^{-4}T^3 + 3.6 \times 10^{-7}T^4, T \in [273K, 553K] \tag{15}$$

$$\lambda_w = -0.869 + 0.009T - 1.584 \times 10^{-5}T^2 + 7.975 \times 10^{-9}T^3, T \in [273K, 553K] \tag{16}$$

$$\mu_w = \begin{cases} 1.38 - 0.021T + 1.36 \times 10^{-4}T^2 - 4.645 \times 10^{-7}T^3 + 8.9 \times 10^{-10}T^4 \\ \quad -9.08 \times 10^{-13}T^5 + 3.85 \times 10^{-16}T^6, T \in [273K, 413K] \\ 0.004 - 2.1075 \times 10^{-5}T + 3.8578 \times 10^{-8}T^2 \\ \quad -2.3973 \times 10^{-11}T^3, T \in [413K, 553K] \end{cases} \tag{17}$$

where ρ_w is the density of water; C_{pw} is the isobaric heat capacity of water; λ_w is the thermal conductivity of water; μ_w is the dynamic viscosity of water.

For simulating the multiphysics interaction behaviors in EGS, the above governing Eqs. (1–17) are all constructed on COMSOL Multiphysics®, and all these equations can be solved simultaneously to achieve fully coupled modeling. The software is a general-purpose numerical solver for partial differential equations based on the finite element method. In this paper, we employ the Newton iteration method to solve the above equation system with a PARDISO direct solver. The time discretization is achieved through a backward difference fully implicit scheme, and the solver adopts an adaptive time stepping approach, with a maximum time step size limit of 0.1 a. When the difference in dependent variables between two iteration steps is less than the tolerance, the iteration is considered convergent. Then we start solving the next time step with a stringent tolerance of 1.0×10^{-4} to guarantee computational precision.

3. Model validation

The objective of this part is to validate the numerical model against analytical solutions, encompassing a 2D transient heat transfer problem between matrix and fracture, and a one-dimensional non-isothermal thermal consolidation model. These models correspond to the TH and THM coupling components of our numerical model, respectively.

3.1. Transient heat transfer problem between matrix and fracture

To assess the reliability of the TH coupling component within our numerical model, the transient heat transfer problem between the fracture and matrix has been specifically chosen as the research object. As depicted in the model's schematic (cf. Fig. 2), the fracture is sandwiched between the upper and lower surrounding rocks. Initially, both the fracture and the matrix share the same temperature. Subsequently, a low-temperature fluid enters the system through the left boundary of the fracture and exits through the right boundary. The model adopts thermal insulation boundaries. The analytical model assumes that the rock matrix is impermeable, allowing fluid flow exclusively along the fracture. Additionally, there is no external heat source within the system. It is assumed that the temperature of the fluid and rock matrix on the fracture are identical, which adheres to the continuity condition.

The normalized temperature of the rock matrix is described by [27,45]

$$T_{sD}(x,y,t) = \frac{T_0 - T}{T_0 - T_{in}} = \mathrm{erfc}\left[\frac{k_s x + \frac{1}{2}d_f v\rho_w c_w |y|}{d_f v\rho_w c_w}\sqrt{\frac{v\rho_s c_s}{k_s(vt-x)}}\right] \tag{18}$$

The normalized temperature of the fracture fluid is described by [27,45]

$$T_{fD}(x,0,t) = \frac{T_0 - T}{T_0 - T_{in}} = \mathrm{erfc}\left[\frac{k_s x}{d_f v\rho_w c_w}\sqrt{\frac{v\rho_s c_s}{k_s(vt-x)}}\right] \tag{19}$$

where T_0 is the initial temperature; T is the current temperature; T_{in} is the temperature of the injected fluid. The erfc() function represents the Gaussian error function. The elucidation and numerical values of additional physical quantities existing in the expression are listed in Table 1.

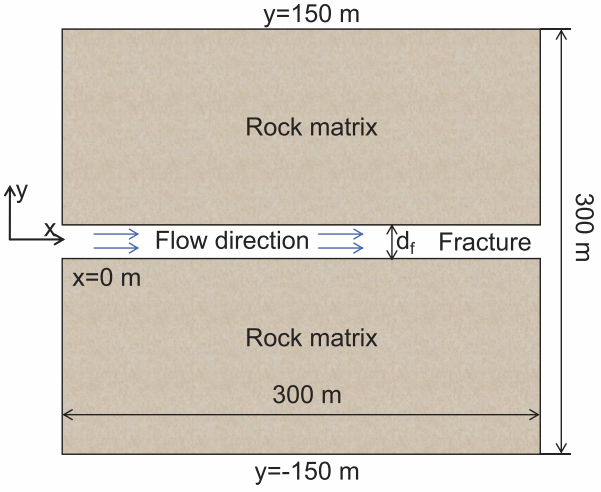

Fig. 2. The schematic diagram of the transient heat transfer problem, with a domain size of 300 m × 300 m.

Table 1
Parameters used for transient heat transfer problem.

Parameter	Value	Description
d_f	3.0 mm	Width of fracture
k_s	2.6 W/m/K	Thermal conductivity of solid matrix
ρ_s	2650 kg/m^3	Density of solid matrix
c_s	1046 J/kg/K	Heat capacity of solid matrix
ρ_w	1000 kg/m^3	Density of fluid
c_w	4200 J/kg/K	Heat capacity of fluid
v	0.5 cm/s	Flow velocity
T_0	300 °C	Initial temperature
T_{in}	20 °C	Temperature of injected fluid

Fig. 3 compares the temperature profiles of the matrix and fracture, indicating good agreement between the numerical and analytical solutions. This comparison validates the reliability of the TH coupling component within the numerical model.

3.2. One-dimensional non-isothermal consolidation model

The model domain is presented in Fig. 4, in which the top surface of the soil pillar is subjected to both external loads and heating. The research object of the non-isothermal consolidation model is saturated soil, which describes the process of gradual dissipation of pore pressure and gradual compaction of the soil. This analytical model assumes there is no time for the soil to deform at the moment of loading, such that the initial displacement is zero and the initial pore pressure is equal to the external load. For the seepage field, the bottom and lateral boundaries are impermeable, and the top is the drainage boundary with zero pressure. For the displacement field, the bottom and lateral boundaries are roller boundaries (no normal displacement), and the top is a stress boundary condition. For the temperature field, the top is the Dirichlet boundary (fixed temperature), and the other boundaries are thermal insulation boundaries. The specific expression of the analytical solution can be found in Bai [50]. Fig. 5 compares the numerical solution with the analytical solution for pore pressure, vertical displacement, and temperature at different times and locations. The results indicate that the numerical solution matches the analytical solution quite closely, verifying the reliability of the THM coupling component of our numerical model. The simulation parameters are listed in Table 2.

4. Applications and results

This section strives to implement the established coupled THM model in a representative 3D geothermal exploitation scenario. We focus on the intricate multiphysics interaction mechanisms that underlie the long-term geothermal extraction process, such as the propagation of pore pressure, the development of the temperature field, and the uneven permeability evolution of fractures.

4.1. Model descriptions

Fig. 6 illustrates the model's schematic diagram, incorporating a double well system. The fracturing zone measures 1000 m × 1000 m × 500 m, corresponding to the x-, y-, and z-direction, respectively. Inside this reservoir, two sets of orthogonal fractures are located. The transverse fractures (aligned with the x-direction) have an initial width of 1.0 mm and the longitudinal ones (aligned with the y-direction) have an initial width of 0.1 mm.

Concerning the initial conditions, it is assumed that the HDR reservoir is initially devoid of fluid, resulting in a zero initial pore pressure. The initial reservoir temperature is set at 250 °C. Regarding the boundary conditions, for the seepage field, all external boundaries, excluding the injection and production wells, are considered impermeable. This assumption is generally considered reasonable, given that the non-fractured zones of the HDR reservoir typically consist of dense bedrock exhibiting extremely low permeability [48]. The injection well operates with an injection rate of 100 kg/s, while the production well remains connected to the atmosphere, maintaining a pressure of 1.0

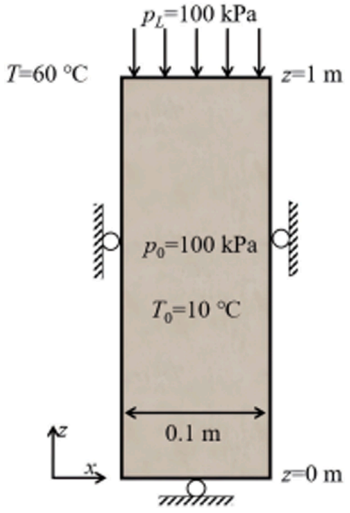

Fig. 4. The schematic diagram and its boundary conditions of the non-isothermal thermal consolidation model.

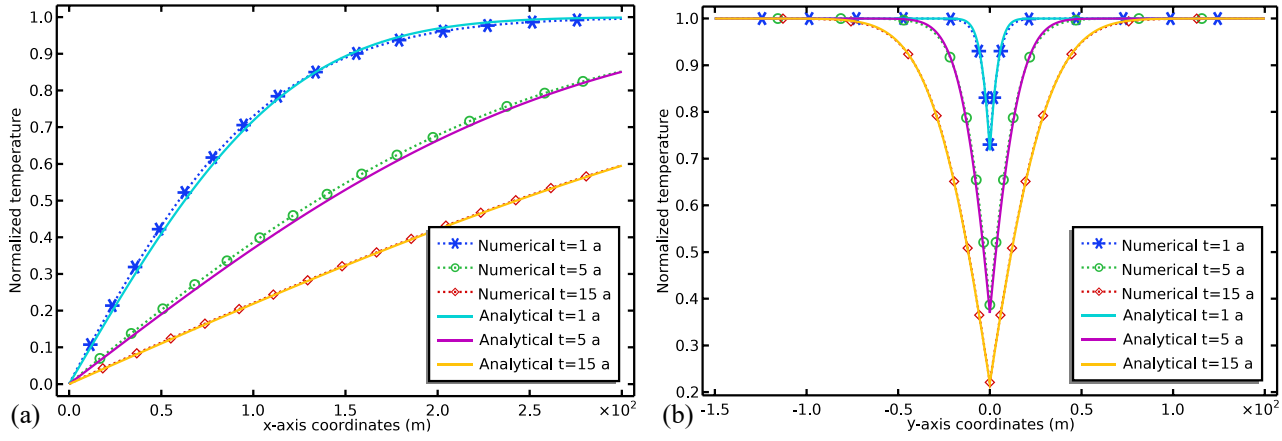

Fig. 3. Comparison of numerical and analytical solutions for the heat transfer problem between matrix and fracture. (a) Distribution of fluid temperature within the fracture along the x-axis; (b) distribution of matrix temperature along the y-axis at x = 100 m. The dashed lines depict numerical solutions, while solid lines represent analytical solutions.

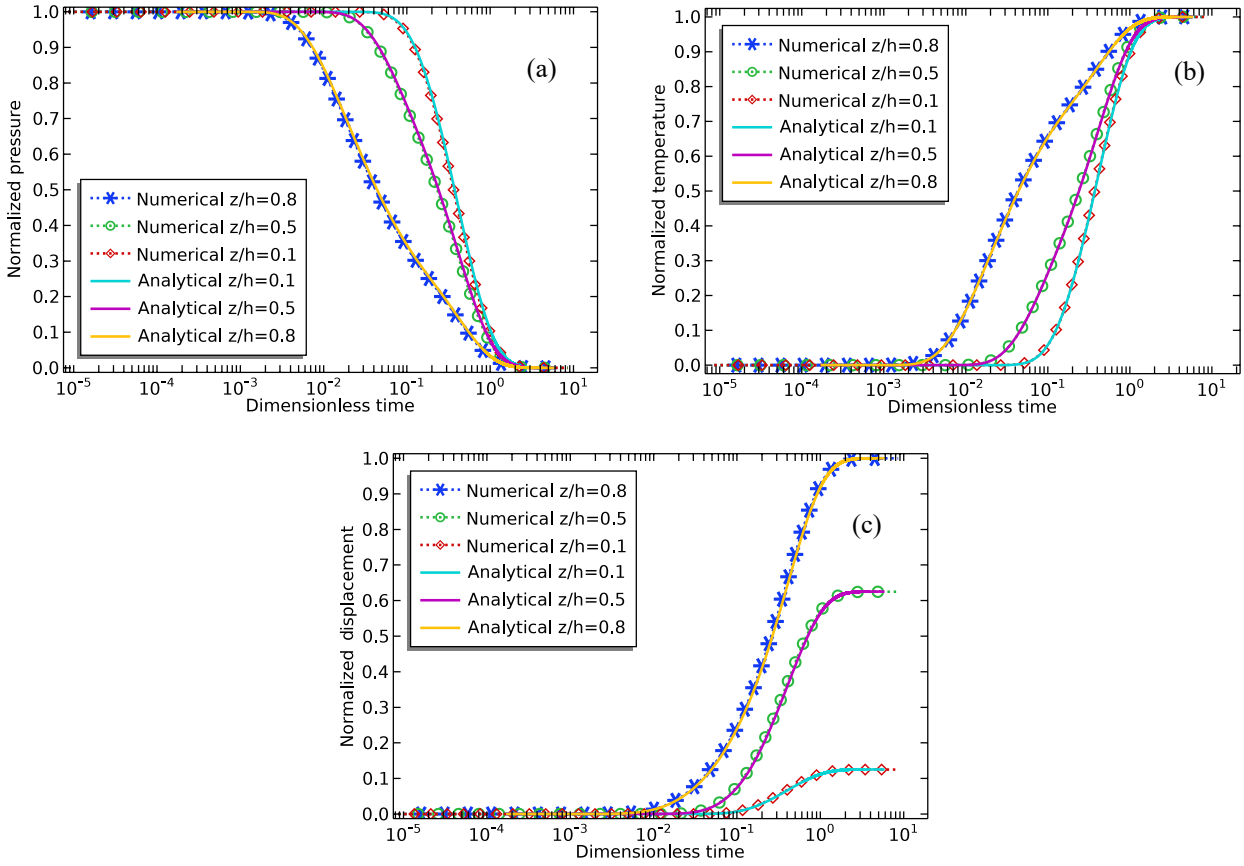

Fig. 5. Comparison of numerical results and analytical solution of non-isothermal consolidation problem for (a) pore pressure, (b) temperature, and (c) vertical displacement. The dashed line represents the numerical solution, and the solid line represents the analytical solution.

Table 2
Parameters used for non-isothermal consolidation problem.

Parameter	Value	Description
h	1.0 m	Model size
α_s	1.5×10^{-5} K^{-1}	Thermal expansion coefficient of soil particle
α_f	2.0×10^{-4} K^{-1}	Thermal expansion coefficient of water
p_L	100 kPa	Magnitude of loading force
E	6.0×10^5 Pa	Elastic modulus
ν	0.3	Poisson's ratio
b	1	Biot coefficient
ϕ	0.4	Porosity
K	2.07×10^{-9} m/s	Hydraulic conductivity
ρ_w	1000 kg/m^3	Density of water
ρ_s	2600 kg/m^3	Density of soil particle
k_{eff}	0.5 W/m/K	Thermal conductivity of soil
c_w	4200 J/kg/K	Specific heat capacity of water
c_s	800 J/kg/K	Specific heat capacity of solid particle
p_0	100 kPa	Initial pore pressure
T_0	10 °C	Initial temperature
T	60 °C	External temperature

atm. For the displacement field, roller boundary conditions are imposed at the lateral and bottom boundaries, with the top surface remaining free to move. The temperature field is thermally insulated, with the injected fluid maintained at 60 °C. Additionally, a line heat source is distributed at the injection well, i.e.,

$$Q_T = C_{pw} \times M_{in} \times (T_{in} - T) \tag{20}$$

where M_{in} is the injection rate; T_{in} is the temperature of injected fluid; T is the ambient temperature at the injection point. Table 3 lists the detailed parameters required for this model.

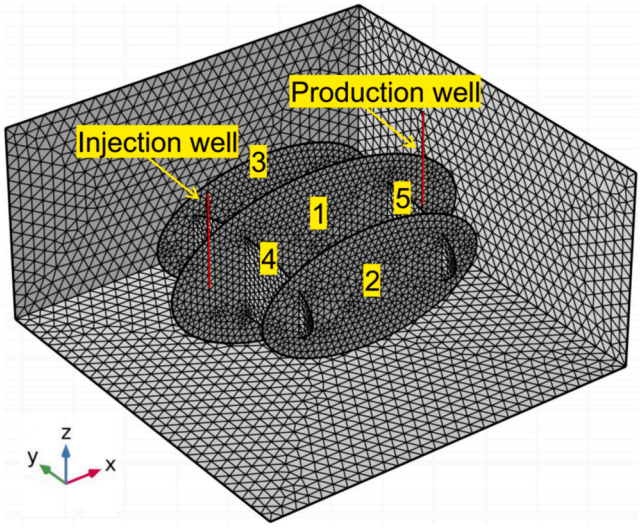

Fig. 6. Schematic and grid division diagram of the 3D geothermal exploitation model, measuring 1000 m × 1000 m × 500 m in size. The numerals within the figures represent the individual fracture numbers.

4.2. Results of the 3D geothermal extraction model

Fig. 7 illustrates the trend of pore pressure changes within the fractures. As time passes, the fractures gradually become interconnected by the injected fluid, resulting in a gradual increase in pore pressure within the fractures. Since the injection well is located on the central main fracture (cf. fracture NO. 1 in Fig. 6), the pore pressure growth within

Table 3
Parameters used for the 3D geothermal extraction model.

Parameter	Value	Description
E	10 GPa	Elastic modulus
v	0.3	Poisson's ratio
b	1	Biot coefficient
ρ_s	2500 kg/m^3	Density of solid matrix
α_m	2.0×10^{-5} K^{-1} [52]	Thermal expansion coefficient of rock mass
k	1.0×10^{-13} m^2	Permeability of the porous matrix
ϕ	0.1	Porosity of porous matrix
ϕ_f	0.7	Porosity of the fracture
S	5.4×10^{-11} Pa^{-1} [25]	The water storage coefficient within matrix
S_f	1.0×10^{-12} Pa^{-1} [25]	The water storage coefficient within fracture
m	1.0×10^{-7} Pa^{-1} [48]	Constitutive constant of fracture's permeability
λ_s	3.0 W/m/K [27]	Thermal conductivity of solid matrix
c_s	800 J/kg/K	Specific heat capacity of solid matrix
T_0	250 °C	Initial temperature
T_{in}	60 °C	Temperature of injected fluid
M_{in}	100 kg/s	Flux of the injection well
P_{pro}	1.0 atm	Pressure of the production well

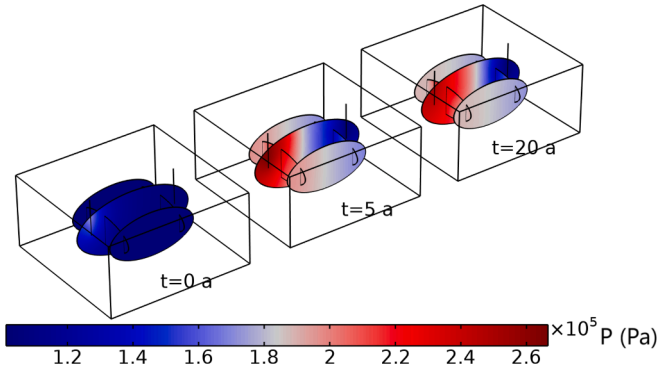

Fig. 7. Evolution of pore pressure within fractures.

this fracture is more significant compared to other fractures.

Fig. 8 illustrates the temperature field evolution in the coupled THM model. Under the THM framework, it becomes evident that the central main fracture experiences a more thorough cooling process, whereas the neighboring fractures (cf. fracture NO. 2 and NO. 3 in Fig. 6) retain higher temperatures. This observation implies that the neighboring fractures lack effective thermal communication, suggesting that the overall heat extraction performance of the reservoir appears to be sub-optimal. This phenomenon is further highlighted in Fig. 9, which

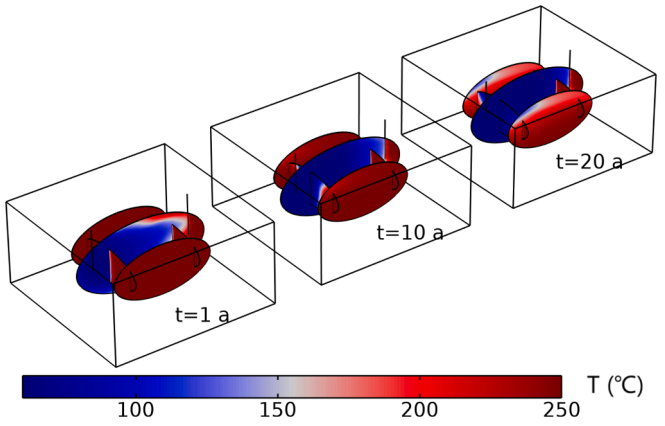

Fig. 8. Evolution of temperature field within fractures under the coupled THM framework.

exhibits a more pronounced distribution of the 3D low-temperature zones within the reservoir.

Fig. 9 exhibits the 3D isothermal surfaces of the reservoir after 20 years of exploitation, revealing the distribution of low-temperature regions both within and surrounding the fractures. Under the coupled THM framework, the cooler zones are primarily clustered around the injection well and the central main fracture. However, the temperatures surrounding other fractures fail to exhibit significant decreases, with only localized cooling observed on these fractures (cf. fracture NO. 2 and NO. 3 in Fig. 6). In extreme cases, fracture NO. 5 remains completely devoid of any thermal communication throughout the entire thermal mining process. Consequently, the isothermal surfaces outlining the low-temperature zones do not form a comprehensive enclosure around these fractures, indicating a significant lack of thermal communication between fractures.

We are intrigued by the underlying reasons for the poor performance of geothermal exploitation. In this regard, Fig. 10 offers valuable insights into the changes in fracture swarm permeability. As fluid is injected, the permeability of the fractures experiences a notable increase compared to their initial states and exhibits a strong dependency on the temperature. For instance, from t = 0 a to t = 5 a, fracture NO. 4 in Fig. 6, indicated by the yellow arrow-marked area, exhibits a distinct trend. As the temperature in this region decreases, the fractures widen due to rock contraction, leading to a gradual enhancement of permeability in this area. Moving from t = 10 a to t = 20 a, the region experiencing permeability growth because temperature reduction expands significantly, and the permeability evolution closely mirrors the temperature variations observed in Fig. 8. Conversely, fracture NO. 2 in Fig. 6, indicated by the blue arrow-marked area, shows only minor growth in permeability compared to the initial state, suggesting limited rock contraction in this region. The limited contraction is attributed to the minimal temperature decrease in this region, which is consistent with the temperature distribution depicted in Fig. 8. Consequently, it is implied that fluid flow through this fracture is insignificant.

Additionally, the final permeability of fractures exhibits remarkable heterogeneity. Initially, two fracture sets differed in permeability by two-orders-of-magnitude due to natural width difference. However, after 20 years of geothermal exploitation, the permeability range broadened significantly, with a four-order-of-magnitude difference between the extremes. As shown in Fig. 10, the maximum permeability (1.14×10^{-6} m^2) occurs near the injection well, where the fluid pressure increases most significantly, and the temperature decreases most thoroughly. The lowest permeability (4.14×10^{-10} m^2) observed at the fracture's edge, as shown in Fig. 11, indicates that this edge is not the primary fluid flow path, experiencing limited impact from temperature and fluid pressure changes. Overall, under the dual effects of fluid injection and temperature decrease, the inherent heterogeneity of natural fractures is further exacerbated.

Fig. 11 provides a detailed snapshot of the flow field distribution within the fractures after 20 years of geothermal exploitation. One of the most noteworthy features is the existence of distinct preferential seepage paths, primarily characterized by the central main fracture. Fracture NO. 1 in Fig. 6, exhibits remarkable permeability. This exceptional permeability translates into high flow velocities (approximately 0.72 m/s) and significant fluxes within the fracture. Consequently, most of the fluid is observed to flow directly along this central fracture from the injection well to the production well, potentially shortening the thermal breakthrough time. However, it is important to note that there are also instances of extreme variation in flow velocities within the fractures. For instance, Fracture NO. 5 exhibits an extremely low flow velocity of merely 0.021 cm/s. This minimal velocity indicates that the fluid scarcely flows through this particular fracture, suggesting a limited role in the overall fluid flow system. This variation in flow velocities depicted in Fig. 11 highlights the complexity of fluid dynamics within the fractured geothermal reservoir. Meanwhile, this figure vividly demonstrates how the pronounced heterogeneity in fracture permeability shapes the

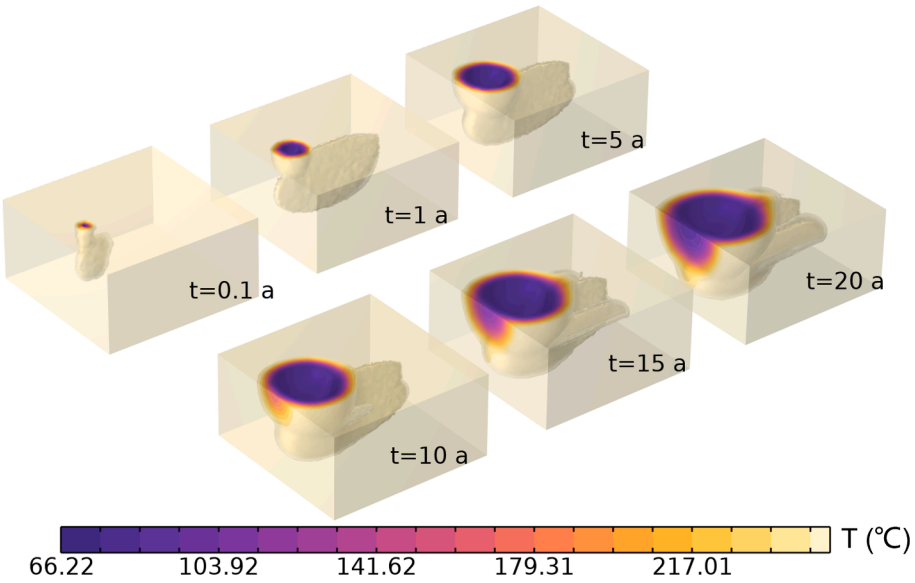

Fig. 9. The 3D isothermal surfaces of the reservoir under the coupled THM framework.

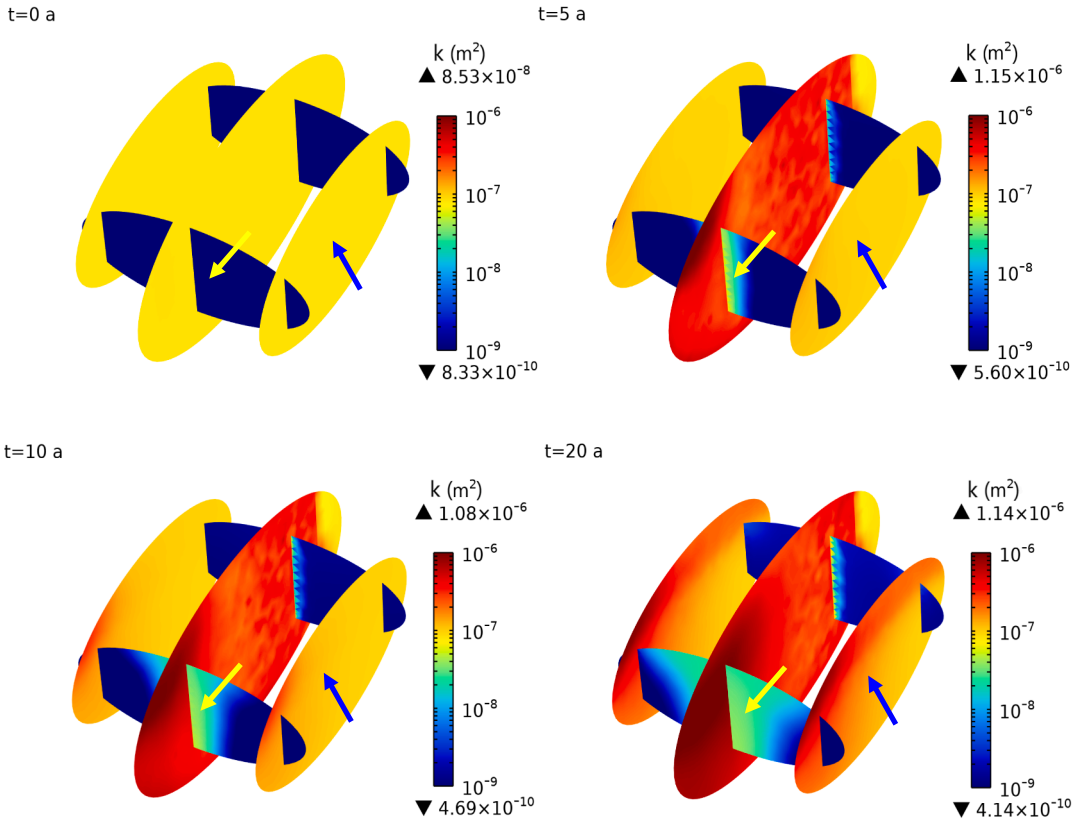

Fig. 10. Evolution of the fractures' permeability field under the coupled THM framework. The yellow arrow-marked region underwent a pronounced cooling effect, accompanied by a remarkable enhancement in permeability. In contrast, the blue arrow-marked region experienced limited cooling, manifesting in a less notable increase in permeability. (For interpretation of the references to colour in this figure legend, the reader is referred to the web version of this article.)

seepage paths within the fracture network.

The emergence and development of preferential flow paths are rooted in deeper mechanisms. As pore pressure increases and temperature decreases, fractures dilate, resulting in enhanced permeability. Subsequently, the increased permeability further elevates fluid velocity, attracting a larger influx of low-temperature fluids into fractures, leading to a more thorough cooling process. This comprehensive cooling of specific fractures, in turn, exaggerates matrix shrinkage and promotes further dilation of these fractures. This positive feedback loop, as depicted in Fig. 12, potentially results in progressively stronger permeability within specific fractures, ultimately leading to a vicious cycle that amplifies the heterogeneity of fractures' permeability. This positive feedback mechanism could provide explanations for the short-circuits phenomenon [11,51] reported by others, which refers to the

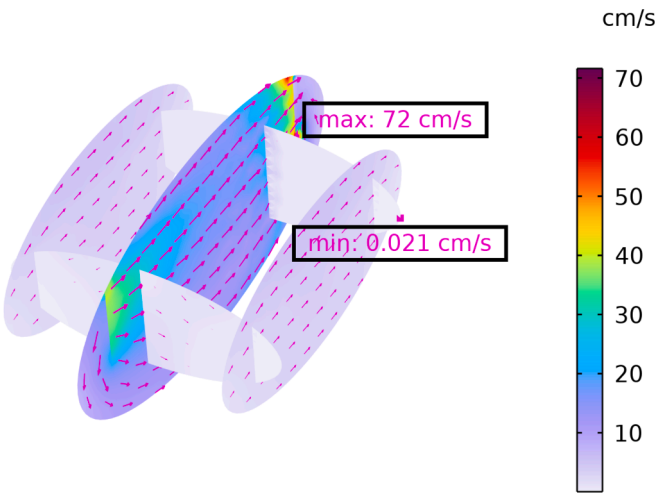

Fig. 11. The final flow field distribution within the fractures at t = 20 a, with the length and density of arrows indicating the magnitude of flow velocity and flow rate.

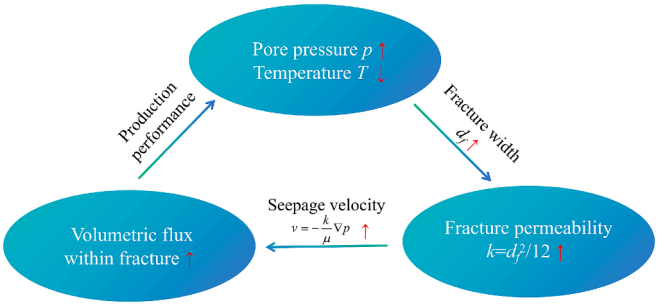

Fig. 12. Schematic diagram of the positive feedback mechanism for the evolution of fracture permeability.

formation of undesirable dominant preferential flow pathways that lead to reduced energy production rates. Furthermore, as shown in Fig. 13 below, the positive feedback mechanism is evidenced by the monotonic growth trend of the fractures' average permeability.

Fig. 13 illustrates the temporal variation of average permeability and mass flow rate within each fracture. Initially, fractures NO. 1, NO. 2, and NO. 3 exhibits identical permeability levels. However, due to favorable spatial positioning, fracture NO. 1, proximal to the injection well, receives a significantly higher flow rate, accounting for approximately 70 % of the total injected flow. This concentration flow augments the permeability of fracture NO. 1, resulting in a significantly greater increase compared to the other fractures. As a result, throughout the mining process, fracture NO. 1 maintains its dominant position in fluid flow with consistently high internal flow rates.

On the other hand, fractures NO. 2 and NO. 3, due to their geometric symmetry, exhibit comparable evolution patterns. While their flow rates and permeability are lower than those of fracture NO. 1, they still exceed the performance of fractures NO. 4 and NO. 5, thanks to their larger initial widths. Notably, despite having a relatively narrow initial width, fracture NO. 4 benefits from significant temperature reduction in the later stage of geothermal extraction, leading to a noteworthy increase in permeability compared to fracture NO. 5. In contrast, fracture NO. 5 scarcely receives any benefit from the low-temperature fluid flow during the mining process, resulting in minimal growth in its permeability. Consequently, both its flow rate and permeability remain at the lowest levels. In summary, the spatial positioning of fractures and their interaction with the injected fluid significantly influenced their permeability and flow characteristics, giving rise to preferential flow paths and varying degrees of fluid extraction efficiency.

5. Discussion

In this section, we conduct a multi-factor comparative analysis to investigate potential factors affecting EGS lifetime, including fracture heterogeneity, local thermal non-equilibrium effect, and layout strategies, as shown in Fig. 1. The example from Section 4 as a benchmark case corresponds to Case 1 in Table 4. Our primary focus is to delve into the significance of the stress field in geothermal mining. Additionally, we investigate whether the preferential flow paths within the fracture network can be optimized under various injection-production scenarios. Furthermore, we compare the performance of LTE and LTNE in long-term geothermal extraction indicators, aiming to explore how different priorities should be assigned to these various influencing factors in EGS lifetime assessment.

5.1. Comparison of heat extraction performance: TH vs THM models

The preceding coupled THM analysis demonstrates that the emergence of preferential flow paths is critically influenced by the stress field, including the pore pressure and the thermal stress. In the EGS design, another common approach is the simplified TH modeling. By neglecting the stress field's influence, it becomes easier and faster to provide assessment results. To investigate whether the stress field truly plays an important role, it is necessary to set up a control experiment, i.e., comparing the thermal extraction performance of the TH and THM models is required.

Fig. 14 presents the results of the coupled TH model, with key parameters referenced from Case 2 in Table 4. After 20 years of extraction, it becomes evident that the cooled area of the fractures is considerably more extensive in the TH model compared to the THM model. The contrast between the low-temperature zones in fractures NO. 2 and NO. 3 is particularly striking (cf. Fig. 8), indicating stronger thermal communication between fractures in the TH model. Moreover, it is noteworthy that during the initial year of operation (t = 1 a), the TH model exhibits a significantly smaller low-temperature region around the central main fracture (cf. fracture NO. 1 in Fig. 6) compared to the THM model. This implies that under the TH mode, the reservoir is less prone to thermal breakthrough. Unlike the THM model, the TH model overlooks fracture permeability evolution, resulting in a less pronounced heterogeneity of the fractures. Consequently, the influence of preferential flow paths is weakened, leading to a delayed thermal breakthrough time and a more uniform cooling effect throughout the reservoir.

Fig. 15 illustrates the evolution of the 3D low-temperature zone in the reservoir using the TH model. Compared to the THM model (cf. Fig. 9), the isotherm contours in the TH model appear more full-bodied. After 20 years of extraction, the isotherm surfaces form a complete closure, encompassing all fractures and fostering a more uniform and balanced cooling effect throughout the reservoir. This heat extraction pattern aligns more closely with our expectations.

Furthermore, it is necessary to evaluate the heat extraction performance using specific quantitative indicators. We then compare the performance of the two models in terms of two key aspects: average production well temperatures and geothermal extraction efficiency. They are defined as follows respectively [53],

$$T_{out} = \frac{\int_L T(t)dl}{L} \tag{21}$$

$$\eta = \frac{\iiint_V \rho_s C_{p,s}(T_0 - T(t))dV}{\iiint_V \rho_s C_{p,s}(T_0 - T_{in})dV} \tag{22}$$

where L represents the total length of the production well section; V stands for the total reservoir volume; $T(t)$ denotes the current

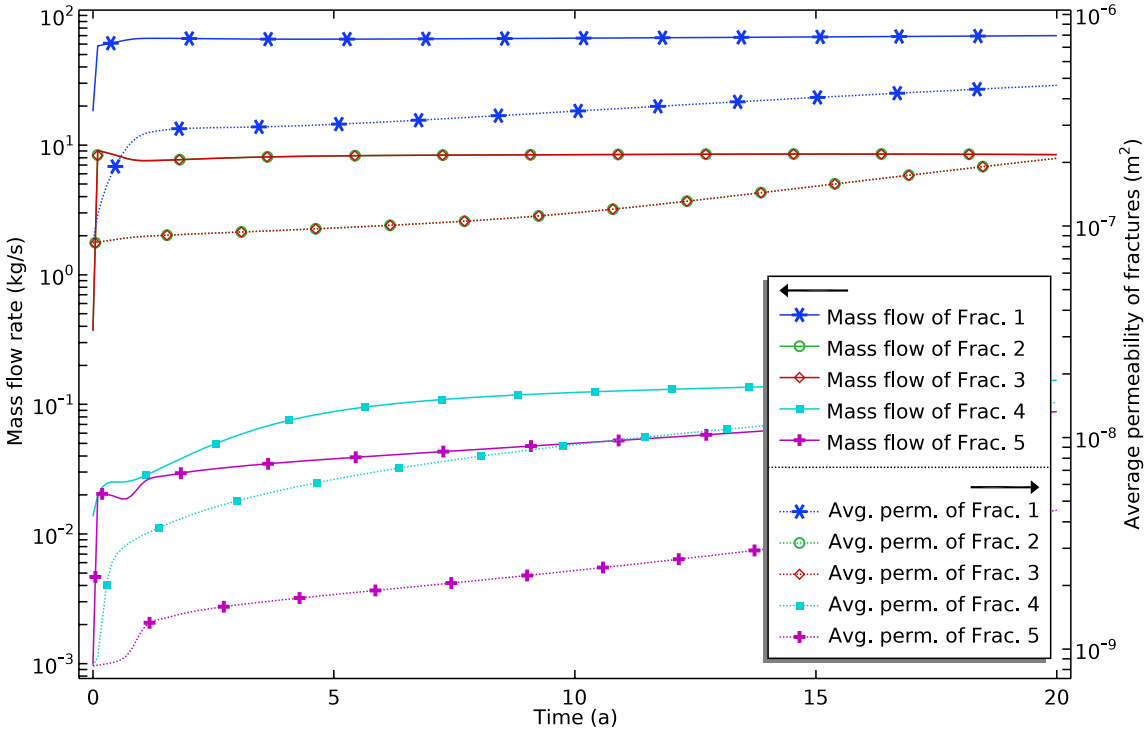

Fig. 13. The evolution of mass flow rate and average permeability for each fracture. The location of the fractures can be referred to in Fig. 6. The solid lines represent the mass flow rate, while the dashed lines represent the average permeability.

Table 4
Some cases and key parameters of 3D geothermal models.

Cases	Injection conditions	Production well temperatures	Effective heat extraction rate	Thermal equilibrium hypothesis	Coupling mode	Total degrees of freedom	Time consuming
Case 1	100 kg/s	140 °C	13 %	LTE	THM Coupling	4,54,005	55 min
Case 2	100 kg/s	188 °C	19 %	LTE	TH Coupling	84,668	7 min
Case 3	200 kg/s	113 °C	22 %	LTE	THM Coupling	4,54,005	55 min
Case 4	300 kg/s	95 °C	28 %	LTE	THM Coupling	4,54,005	55 min
Case 5	3 × 33.3 kg/s	174 °C	19 %	LTE	THM Coupling	4,54,686	55 min
Case 6	100 kg/s	188 °C	19 %	LTNE	TH Coupling	1,26,996	29 min

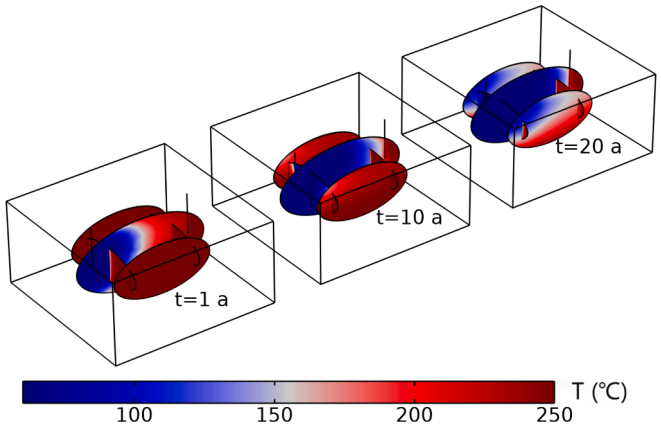

Fig. 14. Evolution of the temperature field within fractures under the coupled TH framework.

temperature; T_0 and T_{in} represent the initial temperature and the temperature of injected fluid, respectively.

Fig. 16 depicts a comparison of heat extraction performance between the two models. As shown in Fig. 16a, the TH model exhibits a significantly higher production temperature (around 200 °C) compared to the THM model (approximately 140 °C). According to the standard definition of EGS lifetime, this refers to the total duration from the commencement of operations until the temperature of the produced fluid declines to below 60 % of the initial reservoir temperature [36]. After this point, the wells need to be shut down to enable the reservoir to recharge its heat-producing capability by absorbing heat from the deep Earth. Based on this criterion, the TH model indicates that the EGS system exhibits excellent heat cycling performance, with the production temperature remaining stable even after 20 years of mining. In contrast, the THM model reveals a different outcome, where the production temperature approaches the critical threshold of 150 °C within merely four years of mining. This indicates a significantly shorter thermal breakthrough time and an extremely limited lifetime for the EGS project. On the other hand, Fig. 16b compares the effective heat extraction rates

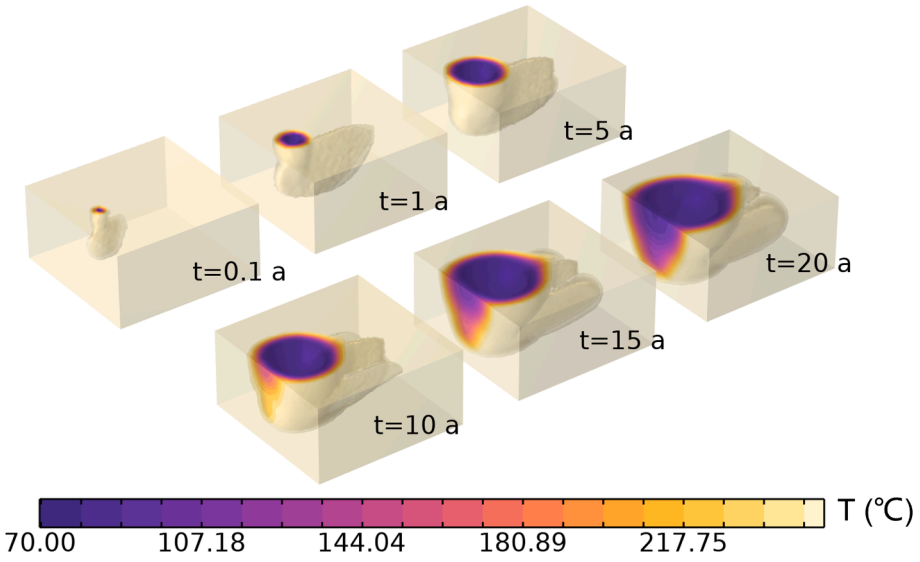

Fig. 15. The 3D isothermal surfaces of the reservoir under the coupled TH framework.

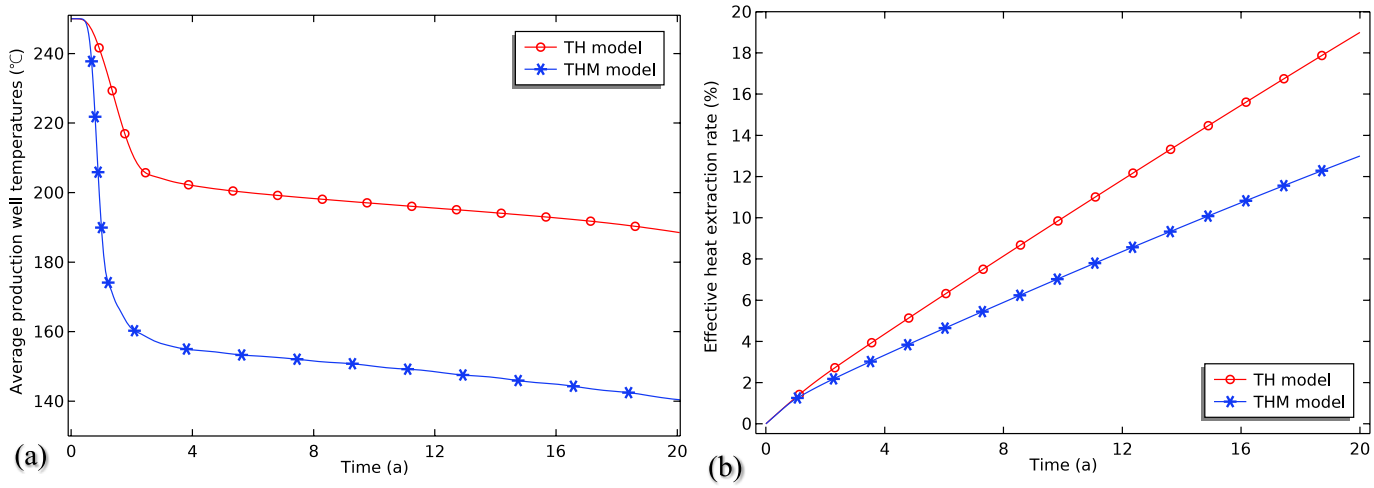

Fig. 16. Comparison of heat extraction effectiveness between TH and THM models: (a) production well temperatures; (b) effective heat extraction rate.

of the two models. Similarly, the TH model consistently yields higher evaluation results than the THM model. This is due to the more efficient heat communication among fractures in the TH model, leading to less significant localized cooling effects, as depicted in the temperature fields of Fig. 14 and Fig. 15. Conversely, in the THM model, the formation of preferential flow paths can easily compromise the heat extraction efficiency.

By comparing Case 1 with Case 2, we recognize that a fracture network with good thermal communication in the TH model may exhibit poor thermal performance from the THM model's perspective. Neglecting the influence of the stress field, the TH model cannot predict the further development of fracture heterogeneity during the mining phase, and fails to capture potential preferential flow paths within the fracture network. This oversight has a profound impact on the timing of thermal breakthroughs and the overall effectiveness of heat extraction. Consequently, simplified TH simulations tend to overestimate geothermal extraction performance.

5.2. Comparison of heat extraction performance: Different well layout strategies

The discussion focuses on whether the emergence of preferential flow paths can be mitigated by adjusting injection and production conditions. As Fig. 17a illustrates, when injection flow rates gradually increase from the scenarios in Cases 1, 3, to 4 of Table 4, there is a certain improvement in the total heat extraction efficiency, rising from 13 % to 28 %. However, a conflicting trend arises: as Fig. 17b shows, with an increase in injection flow rate, the time for thermal breakthrough becomes shorter. The production wells' temperature curves decline more rapidly and steeply, and the final production temperature drops from 140 °C to 95 °C. This poses a dilemma, i.e., while we aim to enhance heat production by increasing injection flow rates, a larger and more concentrated injection tends to facilitate the formation of preferential flow paths. Therefore, we strive to strike a balance between these opposing factors.

In our pursuit of achieving a high heat extraction rate while preventing the development of preferential flow paths that curtail the thermal breakthrough time, we formulate an alternative multi-well scheme, as illustrated in Fig. 18. By maintaining the total injection flow rate equivalent to Case 1, we evenly distribute this flow among three injection wells, corresponding to Case 5 in Table 4. A comparative analysis of Cases 1 and 5 in Fig. 17 underscores that the production temperature and heat extraction rate in Case 5 consistently outperforms those in Case 1. Consequently, implementing the interconnected multi-

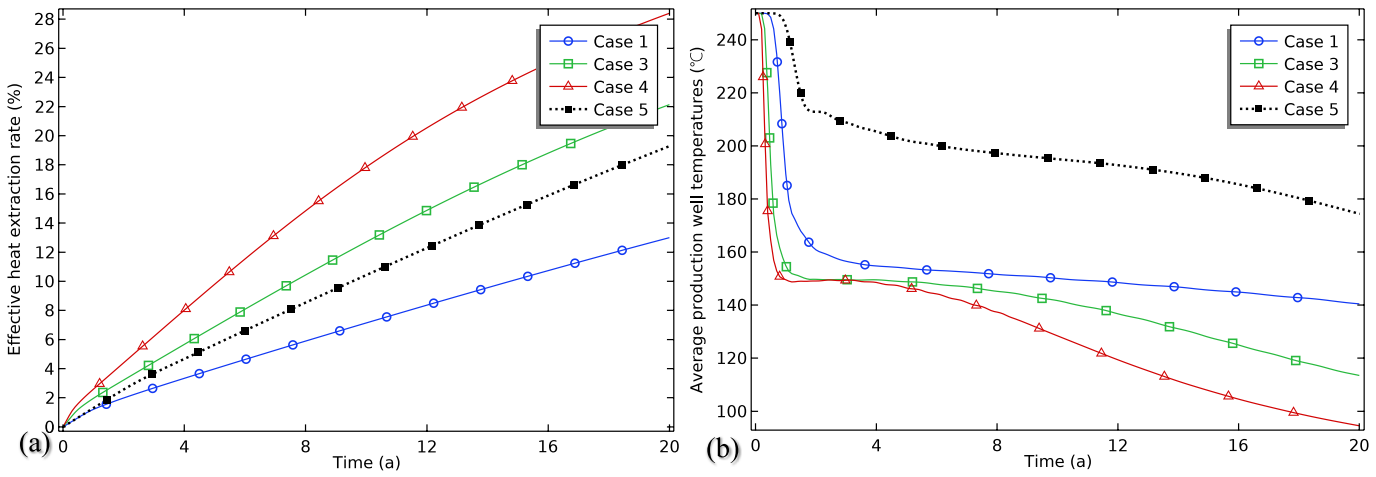

Fig. 17. The heat extraction performance under various injection-production scenarios: (a) effective heat extraction rate; (b) production well temperatures. The solid lines represent the dual-well system, and the dashed lines indicate the multi-well scheme.

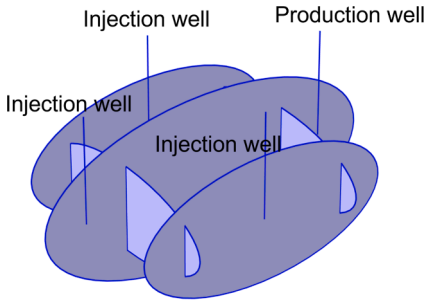

Fig. 18. The schematic diagram of the multi-well integration scheme.

well strategy significantly enhances the overall thermal recovery efficiency of the reservoir, with an identical injection flow rate. While recognizing the additional expenses associated with this approach, its efficacy in extending the EGS lifetime and augmenting its heat production capabilities is considerable. Merely augmenting the injection volume does not substantially improve the fracture network's thermal connectivity; furthermore, it poses a potential risk of fostering preferential flow paths. Thus, adopting the multi-well approach presents a viable solution to balancing these competing factors.

5.3. Comparison of heat extraction performance: LTE vs LTNE models

To investigate the importance of the LTNE effect in affecting the EGS lifetime, we conduct a comparative analysis of the long-term thermal extraction indicators between the LTE and LTNE models, aiming to provide a nuanced understanding of their respective merits and differences. The LTNE model corresponds to Case 6 in Table 4. Fig. 19 shows the results of the dual-temperature fields based on the LTNE model. To capture the distinction in temperatures between the solid and fluid phases, a conservative heat transfer coefficient ($q_{sf} = 5.0$ W/m^3/K [32]) is employed here. The specific quantification of this coefficient and its relevance with LTNE performance can be found in more detailed information in the 'Supporting Materials'. Nonetheless, the LTNE phenomenon does not last for a long time. As illustrated in Fig. 19, during

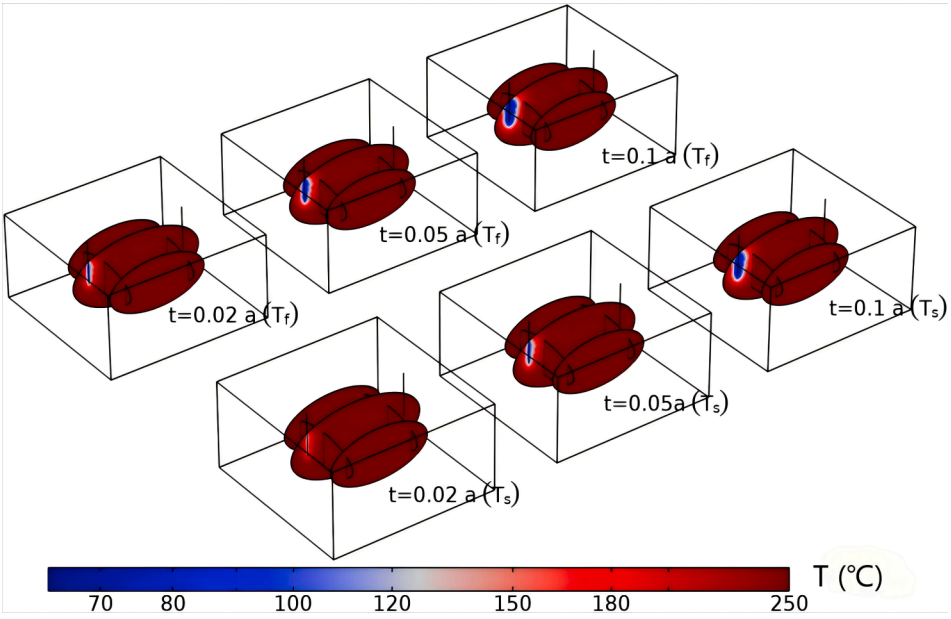

Fig. 19. Variation of the dual temperature field under the LTNE model: fluid temperature field (illustrated in the upper row) and solid temperature field (displayed in the lower one).

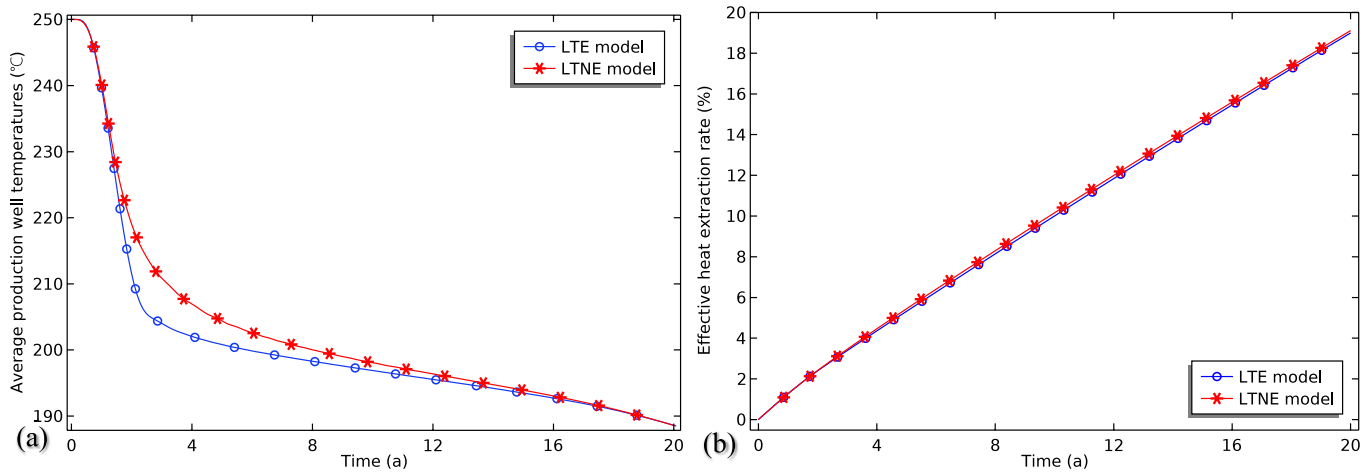

Fig. 20. Comparison of heat extraction effectiveness between LTE and LTNE models: (a) production well temperatures; (b) effective heat extraction rate.

the initial exploitation phase, from 0.02 a to 0.05 a, there remains a discernible difference between the solid-phase temperature and the fluid-phase temperature. Specifically, the fluid temperature within the fracture decreases more rapidly, while the solid-phase temperature lags slightly. However, by 0.1 a, there is no notable temperature difference between the two phases. Jiang et al. [35] also assessed the evolution of the temperature field based on the LTNE framework, and their results showed that the LTNE phenomenon only lasted for 11 days, consistent with the patterns presented here.

Additionally, Fig. 20 presents a more direct and insightful comparison using key quantitative indicators, evaluating the performance of the LTE (Case 2 in Table 4) and LTNE models. Fig. 20 reveals negligible differences in the production temperature curves and virtually identical effective heat extraction rates. Our results indicate that adopting the LTE assumption is satisfactory when the focus is not on localized temperature disparities between solid and fluid phases during the initial exploitation stages, but rather on macro-indicators relevant to long-term geothermal exploitation. Given that EGS systems typically require decades of operational lifetime, short-term localized temperature differences, as illustrated in Fig. 19, are of less consequence. Additionally, we ran these models on a workstation equipped with a 13th Generation Intel® Core™ i7-13700 CPU. With comparable long-term heat extraction outcomes, the LTE model stands out for its reduced degrees of freedom and a faster runtime of just 7 min compared to the LTNE model's 29 min. Since EGS systems are inherently complex, simplifying intricate details with minimal impact on macroscopic results could significantly enhance efficiency in addressing EGS issues. The conservative comparison conducted here does not reveal a significant distinction between the two models. Consequently, our findings support the LTE assumption as a practical reference for the mining of fractured geothermal reservoirs.

On the other hand, Fig. 20a indicates that because of the two calculation methods' inherent differences, the evaluated maximum production temperature differs by approximately 5–8 °C. However, it must be stated that limited by the numerical simulations constraints, this characterization is obtained under current parametric conditions. Therefore, we further introduce a dimensionless number to quantify specific discrepancy degree. The dimensionless production temperature

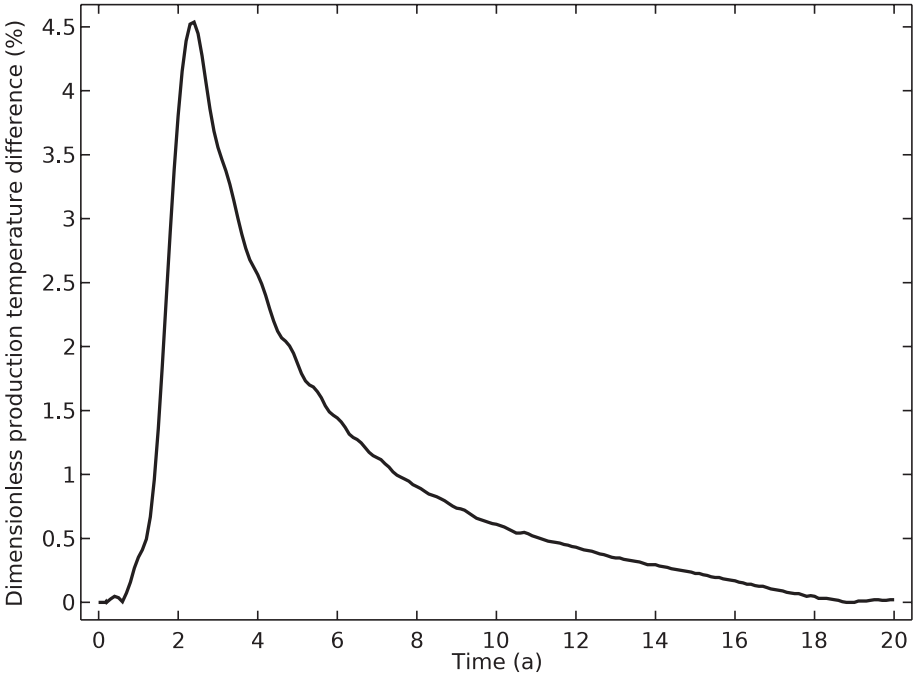

Fig. 21. The difference amplitude of dimensionless production temperature between LTE and LTNE models over time.

difference is defined as [40]

$$\Delta T = \frac{|T_{LTE} - T_{LTNE}|}{T_0 - T_{in}} \times 100\% \quad (23)$$

where T_{LTE} and T_{LTNE} denote the temperature at the production well under local thermal equilibrium and non-equilibrium conditions (Eq. (11)), respectively; T_0 and T_{in} denote the initial reservoir temperature and injection temperature, respectively.

Fig. 21 illustrates the variation of the dimensionless production temperature difference over time, revealing a maximum discrepancy of approximately 4.5 %. The curve's overall trend is one of an initial increase followed by a decrease, with a distinct peak present. Notably, the peak does not persist for an extended period; both the ascent from zero to the peak and the descent from the peak are swift processes. Considering a 20-year complete cycle, the average difference (integral area/total time) is approximately 0.95 %. Both the extremum and the average discrepancy fall within an acceptable range of less than 5 %.

6. Conclusions

In this study, we investigate the permeability evolution mechanism of fracture swarm during geothermal production and its subsequent impact on the lifetime of enhanced geothermal systems. Moreover, we conduct a multi-factor comparative analysis of potential factors, including inherent heterogeneity of fractures, the local thermal non-equilibrium effect, and layout strategies.

Results indicate the strong heterogeneity of the fracture network is dominant, and the intrinsic heterogeneity of fractures is further exacerbated during geothermal production. Specifically, the original permeability difference is two orders, growing to four after 20 years of mining. The underlying reason lies in the combined effects of fluid injection (pore pressure rise) and temperature decrease. A positive feedback mechanism between pore pressure/temperature changes and permeability evolution is observed, leading to monotone permeability-increasing in a limited number of specific fractures, further inducing the formation of preferential seepage paths. This indicates that the uneven permeability evolution of the fracture network is crucial in shortening reservoir lifetime, ignoring fractures' mechanical response leads to an overestimated outcome. A simplified thermal-hydraulic analysis shows a 31 % higher production temperature and a 6 % higher heat extraction rate than the coupled thermo-hydro-mechanical modeling. Simplified thermal-hydraulic analysis indicates that the system can still operate smoothly after 20 years, but the coupled modeling indicates that after 4 years of mining, the production temperature can no longer meet industrial needs. This significant difference emphasizes our attention to fracture deformation during mining.

In contrast, the impact of the local thermal non-equilibrium effect is negligible, with comparable results between equilibrium and non-equilibrium models. The duration of the non-equilibrium phenomenon is very short, spanning a time scale of about tens of days. The dimensionless production temperature difference exhibits a maximum of approximately 4.5 %; when considering the total cycle, the average difference is approximately 0.95 %.

Finally, regarding layout strategies, we find simply boosting injection flow does not fundamentally alter production performance. While tripling the injection flow rate raises the effective heat extraction rate from 13 % to 28 %, geothermal system lifetime evaluation demands more than just one metric. Notably, production well temperatures fall from 140 °C to 95 °C, with a drop of 32 %, which in turn accelerates thermal breakthrough. A multi-well layout helps to alleviate the extremely uneven flow distribution within the fracture network, effectively mitigating the heterogeneity impact and preventing preferential flow paths. Compared to traditional dual-well systems, the multi-well scheme has a 24 % higher temperature and a 6 % higher heat extraction rate. Due to the limitations of numerical simulation research caused by parameter selection, a dimensionless analysis still helps to further generalize the applicability of conclusions.

CRediT authorship contribution statement

Zijun Wei: Investigation, Methodology, Validation, Visualization, Writing – original draft. **Ke Gao:** Formal analysis, Funding acquisition, Project administration, Resources, Software, Supervision, Writing – review & editing. **Sanbai Li:** Formal analysis, Resources, Software, Writing – review & editing.

Declaration of competing interest

The authors declare that they have no known competing financial interests or personal relationships that could have appeared to influence the work reported in this paper.

Acknowledgments

This work is supported by the Shenzhen Science and Technology Program (JCYJ20220530113612028), the Guangdong Basic and Applied Basic Research Foundation (2023A1515011244), and the Guangdong Provincial Key Laboratory of Geophysical High-resolution Imaging Technology (2022B1212010002). Thank you to the editor and reviewers for their constructive suggestions on improving the structure of this paper.

Appendix A

Quantifying the interphase heat transfer coefficient (q_{sf}) in deformable porous media remains an open topic [14]. We introduce a method for quantifying this coefficient, which applies to heat transfer processes occurring between solid particles and fluids within porous packed beds. The heat transfer coefficient, q_{sf}, can be defined as [44]

$$q_{sf} = a_{sf} h_{sf} \quad (24)$$

where a_{sf} represents the specific surface area, and h_{sf} is a transitional heat transfer coefficient. This transitional coefficient is defined as [44]

$$\frac{1}{h_{sf}} = \frac{d_h}{k_f \mathrm{Nu}} + \frac{d_h}{10 k_s} \quad (25)$$

where d_h denotes the characteristic size (hydraulic diameter) of the fracture. In our quantitative calculations, we adopt the parallel plate fracture assumption as a reasonable approximation. Jiang et al. [35] simplified the complex fracture geometry into a parallel plate model, evaluating the specific surface area a_{sf} and the characteristic size of the fracture, and proposed the following relationship, e.g., $a_{sf} = 2\phi/d_f$ and $d_h = 2d_f$.

Moreover, Eq. (25) incorporates a dimensionless fluid-to-solid Nusselt number (Nu). The Nusselt number can be linked to two other dimensionless

numbers: the Prandtl number (Pr), and the Reynolds number (Re). The specific definition is [54]

$$\mathrm{Nu} = 2 + 1.1 Pr^{1/3} \mathrm{Re}^{0.6} \tag{26}$$

with

$$Pr = \frac{\mu C_{p,f}}{k_f}, \qquad \mathrm{Re} = \frac{d_h \rho_f \|\boldsymbol{u}_f\|}{\mu} \tag{27}$$

where $\|\boldsymbol{u}_f\|$ denotes the magnitude of flow velocity within the fracture. The specific calculation process and reference values refer to the details of the 'Supporting Materials'.

Appendix B. Supplementary material

Supplementary data to this article can be found online at https://doi.org/10.1016/j.applthermaleng.2024.124861.

Data availability

Data will be made available on request.

References

[1] J.W. Tester, B. Anderson, A. Batchelor, D. Blackwell, R. DiPippo, E. Drake, et al., The future of geothermal energy: Impact of enhanced geothermal systems (EGS). On the United States in the 21st Century, 2006.

[2] J. Wang, S. Hu, Z. Pang, L. He, P. Zhao, C. Zhu, et al., Estimate of geothermal resources potential for hot dry rock in the continental area of China, Sci. Technol. Rev. 30 (32) (2012) 25–31 [In Chinese].

[3] P. Olasolo, M. Juárez, M. Morales, I. Liarte, Enhanced geothermal systems (EGS): a review, Renew. Sustain. Energy Rev. 56 (2016) 133–144, https://doi.org/10.1016/j.rser.2015.11.031.

[4] C. Xu, P.A. Dowd, Z.F. Tian, A simplified coupled hydro-thermal model for enhanced geothermal systems, Appl. Energy 140 (2015) 135–145, https://doi.org/10.1016/j.apenergy.2014.11.050.

[5] T X, Y Z, Z Z, X B. Advances in exploitation technology of enhanced geothermal system (hot dry rock). Science & Technology Review. 2012;30(32):42-5. [In Chinese].

[6] C.R. Chamorro, J.L. García-Cuesta, M.E. Mondéjar, A. Pérez-Madrazo, Enhanced geothermal systems in Europe: an estimation and comparison of the technical and sustainable potentials, Energy 65 (2014) 250–263, https://doi.org/10.1016/j.energy.2013.11.078.

[7] I. Berre, F. Doster, E. Keilegavlen, Flow in fractured porous media: A review of conceptual models and discretization approaches, Transp. Porous Media 130 (1) (2019) 215–236, https://doi.org/10.1007/s11242-018-1171-6.

[8] L. Jing, A review of techniques, advances and outstanding issues in numerical modelling for rock mechanics and rock engineering, Int. J. Rock Mech. Min. Sci. 40 (3) (2003) 283–353, https://doi.org/10.1016/S1365-1609(03)00013-3.

[9] W. Dershowitz, Hybrid discrete fracture network and equivalent continuum model for shaft sinking, The 41st U.S. Symposium on Rock Mechanics (USRMS), Golden, Colorado, 2006.

[10] S. Joyce, L. Hartley, D. Applegate, J. Hoek, P. Jackson, Multi-scale groundwater flow modeling during temperate climate conditions for the safety assessment of the proposed high-level nuclear waste repository site at Forsmark, Sweden, Hydrgeol. J. 22 (6) (2014) 1233, https://doi.org/10.1007/s10040-014-1165-6.

[11] H.S. Viswanathan, J. Ajo-Franklin, J.T. Birkholzer, J.W. Carey, Y. Guglielmi, J. Hyman, et al., From fluid flow to coupled processes in fractured rock: Recent advances and new frontiers, Rev. Geophys. 60 (1) (2022), https://doi.org/10.1029/2021RG000744.

[12] F. Jiang, L. Luo, J. Chen, A novel three-dimensional transient model for subsurface heat exchange in enhanced geothermal systems, Int. Commun. Heat Mass Transfer 41 (2013) 57–62, https://doi.org/10.1016/j.icheatmasstransfer.2012.11.003.

[13] W. Cao, W. Huang, F. Jiang, A novel thermal-hydraulic-mechanical model for the enhanced geothermal system heat extraction, Int. J. Heat Mass Transf. 100 (2016) 661–671, https://doi.org/10.1016/j.ijheatmasstransfer.2016.04.078.

[14] R. Gelet, B. Loret, N. Khalili, A thermo-hydro-mechanical coupled model in local thermal non-equilibrium for fractured HDR reservoir with double porosity, J. Geophys. Res.: SolidEarth 117 (B7) (2012), https://doi.org/10.1029/2012JB009161.

[15] J. Taron, D. Elsworth, Thermal-hydrologic-mechanical-chemical processes in the evolution of engineered geothermal reservoirs, Int. J. Rock Mech. Min. Sci. 46 (5) (2009) 855–864, https://doi.org/10.1016/j.ijrmms.2009.01.007.

[16] Y.-S. Wu, G. Moridis, B. Bai, K. Zhang, editors. A multi-continuum model for gas production in tight fractured reservoirs. SPE Hydraulic Fracturing Technology Conference and Exhibition. 2009. https://doi.org/10.2118/118944-MS.

[17] M. Mirzaei, C.L. Cipolla, A workflow for modeling and simulation of hydraulic fractures in unconventional gas reservoirs, SPE Middle East Unconventional Resources Conference and Exhibition, 2012. https://doi.org/10.2118/153022-MS.

[18] B. Brian, Characterizing flow and transport in fractured geological media: A review, Adv. Water Resour. (2002), https://doi.org/10.1016/S0309-1708(02)00042-8.

[19] M.C. Cacas, E. Ledoux, G.D. Marsily, B. Tillie, A. Barbreau, E. Durand, et al., Modeling fracture flow with a stochastic discrete fracture network: Calibration and validation: 1. The flow model, Water Resour. Res. 26 (3) (1990), https://doi.org/10.1029/WR026I003P00479.

[20] G. Margolin, B. Berkowitz, H. Scher, Structure, flow, and generalized conductivity scaling in fracture networks, Water Resour. Res. 34 (9) (1998) 2103–2121, https://doi.org/10.1029/98WR01648.

[21] L. Smith, F.W. Schwartz, An analysis of the influence of fracture geometry on mass transport in fractured media, Water Resour. Res. 20 (9) (1984) 1241–1252, https://doi.org/10.1029/WR020i009p01241.

[22] Y. Tsang, C. Tsang, I. Neretnieks, L. Moreno, Flow and tracer transport in fractured media: A variable aperture channel model and its properties, Water Resour. Res. 24 (12) (1988) 2049–2060, https://doi.org/10.1029/WR024i012p02049.

[23] S.H. Lee, M.F. Lough, C.L. Jensen, Hierarchical modeling of flow in naturally fractured formations with multiple length scales, Water Resour. Res. 37 (3) (2001) 443–455, https://doi.org/10.1029/2000WR900340.

[24] Z. Chen, G. Huan, Y. Ma, Computational methods for multiphase flows in porous media, Comput. Sci. Eng. (2006), https://doi.org/10.1137/1.9780898718942.

[25] Z. Sun, X. Zhang, Y. Xu, J. Yao, H. Wang, S. Lv, et al., Numerical simulation of the heat extraction in EGS with thermal-hydraulic-mechanical coupling method based on discrete fractures model, Energy 120 (2017) 20–33, https://doi.org/10.1016/j.energy.2016.10.046.

[26] Z. Sun, Y. Xin, J. Yao, K. Zhang, L. Zhuang, X. Zhu, et al., Numerical investigation on the heat extraction capacity of dual horizontal wells in enhanced geothermal systems based on the 3-D THM model, Energies 11 (2) (2018) 280, https://doi.org/10.3390/en11020280.

[27] J. Yao, X. Zhang, Z. Sun, Z. Huang, J. Liu, Y. Li, et al., Numerical simulation of the heat extraction in 3D-EGS with thermal-hydraulic-mechanical coupling method based on discrete fractures model, Geothermics 74 (2018) 19–34, https://doi.org/10.1016/j.geothermics.2017.12.005.

[28] Z. Lei, Y. Zhang, Q. Cui, Y. Shi, The injection-production performance of an enhanced geothermal system considering fracture network complexity and thermo-hydro-mechanical coupling in numerical simulations, Sci. Rep. 13 (1) (2023) 14558, https://doi.org/10.1038/s41598-023-41745-7.

[29] B. Wu, X. Zhang, R.G. Jeffrey, A.P. Bunger, S. Jia, A simplified model for heat extraction by circulating fluid through a closed-loop multiple-fracture enhanced geothermal system, Appl. Energy 183 (2016) 1664–1681, https://doi.org/10.1016/j.apenergy.2016.09.113.

[30] T. Guo, F. Gong, X. Wang, Q. Lin, Z. Qu, W. Zhang, Performance of enhanced geothermal system (EGS) in fractured geothermal reservoirs with CO_2 as working fluid, Appl. Therm. Eng. 152 (2019) 215–230, https://doi.org/10.1016/j.applthermaleng.2019.02.024.

[31] P. Asai, P. Panja, J. McLennan, M. Deo, Effect of different flow schemes on heat recovery from Enhanced Geothermal Systems (EGS), Energy 175 (2019) 667–676, https://doi.org/10.1016/j.energy.2019.03.124.

[32] Y. Wang, T. Li, Y. Chen, G. Ma, A three-dimensional thermo-hydro-mechanical coupled model for enhanced geothermal systems (EGS) embedded with discrete fracture networks, Comput. Methods Appl. Mech. Eng. 356 (2019) 465–489, https://doi.org/10.1016/j.cma.2019.06.037.

[33] Y. Shi, X. Song, J. Li, G. Wang, R. Zheng, F. YuLong, Numerical investigation on heat extraction performance of a multilateral-well enhanced geothermal system with a discrete fracture network, Fuel 244 (2019) 207–226, https://doi.org/10.1016/j.fuel.2019.01.164.

[34] J.D. Hyman, Flow channeling in fracture networks: Characterizing the effect of density on preferential flow path formation, Water Resour. Res. 56 (9) (2020), https://doi.org/10.1029/2020WR027986.

[35] F. Jiang, J. Chen, W. Huang, L. Luo, A three-dimensional transient model for EGS subsurface thermo-hydraulic process, Energy 72 (2014) 300–310, https://doi.org/10.1016/j.energy.2014.05.038.

[36] T. Guo, S. Tang, J. Sun, F. Gong, X. Liu, Z. Qu, et al., A coupled thermal-hydraulic-mechanical modeling and evaluation of geothermal extraction in the enhanced geothermal system based on analytic hierarchy process and fuzzy comprehensive evaluation, Appl. Energy 258 (2020) 113981, https://doi.org/10.1016/j.apenergy.2019.113981.
[37] W. Minkowycz, A. Haji-Sheikh, K. Vafai, On departure from local thermal equilibrium in porous media due to a rapidly changing heat source: the Sparrow number, Int. J. Heat Mass Transf. 42 (18) (1999) 3373–3385, https://doi.org/10.1016/S0017-9310(99)00043-5.
[38] G.F. Al-Sumaily, H.M. Hussen, M.C. Thompson, Validation of thermal equilibrium assumption in free convection flow over a cylinder embedded in a packed bed, Int. Commun. Heat Mass Transfer 58 (2014) 184–192, https://doi.org/10.1016/j.icheatmasstransfer.2014.08.039.
[39] L. Zhang, F. Luo, R. Xu, P. Jiang, H. Liu, Heat transfer and fluid transport of supercritical CO_2 in enhanced geothermal system with local thermal non-equilibrium model, Energy Procedia 63 (2014) 7644–7650, https://doi.org/10.1016/j.egypro.2014.11.798.
[40] S. Hamidi, T. Heinze, B. Galvan, S.A. Miller, Critical review of the local thermal equilibrium assumption in heterogeneous porous media: Dependence on permeability and porosity contrasts, Appl. Therm. Eng. (2019), https://doi.org/10.1016/j.applthermaleng.2018.10.130.
[41] R. Gelet, B. Loret, N. Khalili, Thermal recovery from a fractured medium in local thermal non-equilibrium, Int. J. Numer. Anal. Meth. Geomech. 37 (2013), https://doi.org/10.1002/nag.2145.
[42] O. Coussy, Poromechanics. John Wiley & Sons. 2004. https://doi.org/10.1002/0470092718.
[43] S. Li, X. Feng, D. Zhang, H. Tang, Coupled thermo-hydro-mechanical analysis of stimulation and production for fractured geothermal reservoirs, Appl. Energy 247 (2019) 40–59, https://doi.org/10.1016/j.apenergy.2019.04.036.
[44] D.A. Nield, A. Bejan, Convection heat transfer, Springer, 2006. https://doi.org/10.1002/9781118671627.
[45] A.D. Cheng, A. Ghassemi, E. Detournay, Integral equation solution of heat extraction from a fracture in hot dry rock, Int. J. Numer. Anal. Meth. Geomech. 25 (13) (2001) 1327–1338, https://doi.org/10.1002/nag.182.
[46] R.G. Carbonell, S. Whitaker, Heat and mass transfer in porous media. Fundamentals of transport phenomena in porous media, Springer. (1984) 121–198, https://doi.org/10.1007/978-94-009-6175-3_3.
[47] S. Miller, Modeling enhanced geothermal systems and the essential nature of large-scale changes in permeability at the onset of slip, Geofluids 15 (1–2) (2015) 338–349, https://doi.org/10.1111/gfl.12108.
[48] Y. Shi, X. Song, J. Li, G. Wang, F. YuLong, L. Geng, Analysis for effects of complex fracture network geometries on heat extraction efficiency of a multilateral-well enhanced geothermal system, Appl. Therm. Eng. 159 (2019) 113828, https://doi.org/10.1016/j.applthermaleng.2019.113828.
[49] Z. Qu, W. Zhang, T. Guo, Influence of different fracture morphology on heat mining performance of enhanced geothermal systems based on COMSOL, Int. J. Hydrogen Energy 42 (29) (2017) 18263–18278, https://doi.org/10.1016/j.ijhydene.2017.04.168.
[50] B. Bai, One-dimensional thermal consolidation characteristics of geotechnical media under non-isothermal conditions, Eng. Mech. 22 (5) (2005) 186–191.
[51] P. Fu, Y. Hao, S.D. Walsh, C.R. Carrigan, Thermal drawdown-induced flow channeling in fractured geothermal reservoirs, Rock Mech. Rock Eng. 49 (2016) 1001–1024, https://doi.org/10.1007/s00603-015-0776-0.
[52] S. Li, X. Li, D. Zhang, A fully coupled thermo-hydro-mechanical, three-dimensional model for hydraulic stimulation treatments, J. Nat. Gas Sci. Eng. 34 (2016) 64–84, https://doi.org/10.1016/j.jngse.2016.06.046.
[53] X. Song, Y. Shi, G. Li, R. Yang, G. Wang, R. Zheng, et al., Numerical simulation of heat extraction performance in enhanced geothermal system with multilateral wells, Appl. Energy 218 (2018) 325–337, https://doi.org/10.1016/j.apenergy.2018.02.172.
[54] N. Wakao, S. Kaguei, T. Funazkri, Effect of fluid dispersion coefficients on particle-to-fluid heat transfer coefficients in packed beds: Correlation of nusselt numbers, Chem. Eng. Sci. 34 (3) (1979) 325–336, https://doi.org/10.1016/0009-2509(79)85064-2.